12-2006

Variational and Partial Differential Equation Models for Color Image Denoising and Their Numerical Approximations using Finite Element Methods

Miun Yoon

To the Graduate Council:

I am submitting herewith a thesis written by Miun Yoon entitled "Variational and Partial Differential Equation Models for Color Image Denoising and Their Numerical Approximations using Finite Element Methods." I have examined the final electronic copy of this thesis for form and content and recommend that it be accepted in partial fulfillment of the requirements for the degree of Master of Science, with a major in Mathematics.

Xiaobing Feng, Major Professor

We have read this thesis and recommend its acceptance:

Charles Collins, Suzanne Lenhart

Accepted for the Council:
Carolyn R. Hodges

Vice Provost and Dean of the Graduate School

(Original signatures are on file with official student records.)

To the Graduate Council:

I am submitting herewith a thesis written by Miun Yoon entitled "Variational and Partial Differential Equation Models for Color Image Denoising and Their Numerical Approximations using Finite Element Methods." I have examined the final electronic copy of this thesis for form and content and recommend that it be accepted in partial fulfillment of the requirements for the degree of Master of Science, with a major in Mathematics.

Xiaobing Feng

Major Professor

We have read this dissertation
and recommend its acceptance:

Charles Collins

Suzanne Lenhart

Accepted for the Council:

Linda Painter

Interim Dean of Graduate Studies

(Original signatures are on file with official student records.)

Variational and Partial Differential Equation Models for Color Image Denoising and Their Numerical Approximations using Finite Element Methods

A Thesis

Presented for the

Masters of Science

Degree

The University of Tennessee, Knoxville

Miun Yoon

December 2006

Dedication

This thesis is dedicated to my parents who raised me with freedom of choice,
to my husband, Kyungyuk, who has always been there,
and to my son, Hagen, who has grown into a wonderful 1 year old boy.

Acknowledgments

I would like to take this opportunity to thank many people who have made this thesis possible. First and foremost, I would like to thank my thesis advisor, Dr. Xiaobing Feng for his guidance and encouragement. Dr. Feng has led me to this very fun field of study and never got tired of answering my questions. I would also like to thank the other members of my committee: Dr. Suzanne Lenhart who gives me great support as a woman mathematician and Dr. Charles Collins who taught me the advanced numerical analysis.

A number of people whom I have met at the UTK deserve my special thanks. Shannon Morrison has encouraged whenever I was depressed. She has always been there as a sister and friend. Allison Carter, who has been my friend longer than any other in this country, has kept me motivated and encouraged when I could not see light at the end of the tunnel. Also, I would like to thank Jane Parker, Pam Armentrout, and Tracy Viles for their support and help. A special thank you should go to Eunjoo Im, Hagen's first nanny and my wonderful Korean friend. She has taken great care of my son. Her contagious smile has given me encouragement and hope during the long hours this thesis has been written. Thank you all for always being there for me.

Finally, I would like to acknowledge the support of the NSF grant DMS-0410266 for my research during the summers of 20005 and 2006.

Abstract

Image processing has been a traditional engineering field, which has a broad range of applications in science, engineering and industry. Not long ago, statistical and ad hoc methods had been main tools for studying and analyzing image processing problems. In the past decade, a new approach based on variational and partial differential equation (PDE) methods has emerged as a more powerful approach. Compared with old approaches, variational and PDE methods have remarkable advantages in both theory and computation. It allows to directly handle and process visually important geometric features such as gradients, tangents and curvatures, and to model visually meaningful dynamic process such as linear and nonlinear diffusions. Computationally, it can greatly benefit from the existing wealthy numerical methods for PDEs.

Mathematically, a (digital) greyscale image is often described by a matrix and each entry of the matrix represents a pixel value of the image and the size of the matrix indicates the resolution of the image. A (digital) color image is a digital image that includes color information for each pixel. For visually acceptable results, it is necessary (and almost sufficient) to provide three color channels for each pixel, which are interpreted as coordinates in some color space. The RGB (Red, Green, Blue) color space is commonly used in computer displays. Mathematically, a RGB color image is described by a stack of three matrices so that each color pixel value of the RGB color image is represented by a three-dimensional vector consisting values

from the RGB channels. The brightness and chromaticity (or polar) decomposition of a color image means to write the three-dimensional color vector as the product of its length, which is called the brightness, and its direction, which is defined as the chromaticity. As a result, the chromaticity must lie on the unit sphere $\mathbf{S^2}$ in $\mathbf{R}^3$.

The primary objectives of this thesis are to present and to implement a class of variational and PDE models and methods for color image denoising based on the brightness and chromaticity decomposition. For a given noisy digital image, we propose to use the well-known Total Variation (TV) model to denoise its brightness and to use a generalized p-harmonic map model to denoise its chromaticity. We derive the Euler-Lagrange equations for these models and formulate the gradient descent method (in the name of gradient flows) for computing the solutions of these equations. We then formulate finite element schemes for approximating the gradient flows and implement these schemes on computers using Matlab® and Comsol Multiphysics® software packages. Finally, we propose some generalizations of the p-harmonic map model, and numerically compare these models with the well-known channel-by-channel model.

Contents

List of Figures

Chapter 1

Introduction

1.1 Digital Image Processing

In modern society, images are powerful information and widely used in numerous fields, such as medical industry, machine vision, and space exploration etc. Because of the complexity and diversity of images, image processing is one of the most challenging areas in mathematics, engineering, medical science, and entertainment industry. Development of computer technology enables us to process images produced by devices such as camera, scanner, ultrasounds, and X-rays to improve their quality, enhance their features, and combine different pieces of information. Any image processor can be presented by an input-output system shown in Figure 1.1, where u_0 is an observed image, which could be degraded due to either poor imaging conditions or problems during storage. Mathematically, an image processor could be any linear or nonlinear operator that processes the input and produces desired output F. The image processor is often developed and designed for specific applications. For instance, one wishes to restore or enhance the observed images which are degraded to obtain high quality images based on other important visual devices, such as tumor detection

Figure 1.1: Image Processor

from lowly contrasted CT images and detecting celestial details from a blurry Hubble telescope image. Image processing could be divided into three main areas. They are image restoration, compression, and segmentation. It is challenge to develope the image processor is challenging because most image processing problems are ill-posed inverse problems, which means that it requires to recover or detect F from u_0. Numerous approaches, such as stochastic modeling, wavelets, variational and PDE modeling, for image processing have been developed in the past thirty years. Modern image processing is qualitatively connected. Stochastic and wavelets, however, are not suitable to preserve sharp edges which define the location of objects. Here, we are interested in variational approach for image processing. PDE models treat images as continuous functions. The PDE models have been successfully used in many areas of image processing including denoising, enhancement, inpainting, and deblurring. The main reason for the successful application of PDEs in image processing is that many variational problems or their regularized approximations can be effectively computed via their Euler-Lagrange equations. In this thesis, we focus on the PDE method for denoising both gray images and color images. In order to understand the process of the noise removal models, it is important to have a good grasp of the mathematical meaning of images.

To give the mathematical definition of images, the concept of pixels needs to be recalled. Pixel is a compound word of **Pic**ture and **El**ement. The monitor divides the screen into thousands of regular grids to display images. We call a regular grid,

a pixel. Thus, images are nothing but a set of numbers given on pixels which are arranged in rows and columns. Images may be defined as a two-dimensional function, $f(x, y)$, where x, y are *spatial* (plane) *coordinates*, and the value of f at any pair of coordinates (x, y) indicates the *intensity* of the images at that point [Gon04]. Therefore, mathematically an image is a matrix whose elements are pixel values. Figure 1.2 shows the representations of an image as a matrix and spatial coordinates.

An RGB color image is an $M \times N \times 3$ array of color pixels, where each pixel is a triplet corresponding to the red, green, and blue components of an RGB image at a specific spatial location. An RGB color image may be viewed as a "stack" of three gray-scale images (see Figure 1.3) that, when fed into the red, green, and blue inputs of a color monitor, produce a color image on the screen [Gon04]. The number of bits used to represent the pixel values of images determines the number of colors and shades of gray to be displayed. Common pixel representations are unsigned bytes (8-bit integers in the range [0,255]) and floating point, that is, there are 256 possible colors or shades of gray-level. An RGB color image has 24-bits information (8-bit per channel). The RGB color image is an additive image which means that red, green, and blue are combined in various ways to produce other colors. Figure 1.4 displays the representation of additive color mixing. Pixel values of RGB color image means "how much" red, green, and blue at the pixel. A color image with 24-bit has 256 shades of red, green, and blue, so that there are 16,777,216 possible combinations of colors. Figure 1.5 shows that the primary and secondary colors of light at the vertices. Red is a composition of RGB values (255, 0, 0) and it is (1, 0, 0) in the RGB color cube. Black is a combination of (0, 0, 0) in RGB color map, and white is a combination of (255, 255, 255). The main diagonal of RGB color cube have gray values from black to white, that is, gray is a combination of equal values of RGB. Since all components in gray are identical in RGB, a gray-scale image only uses 8-bit

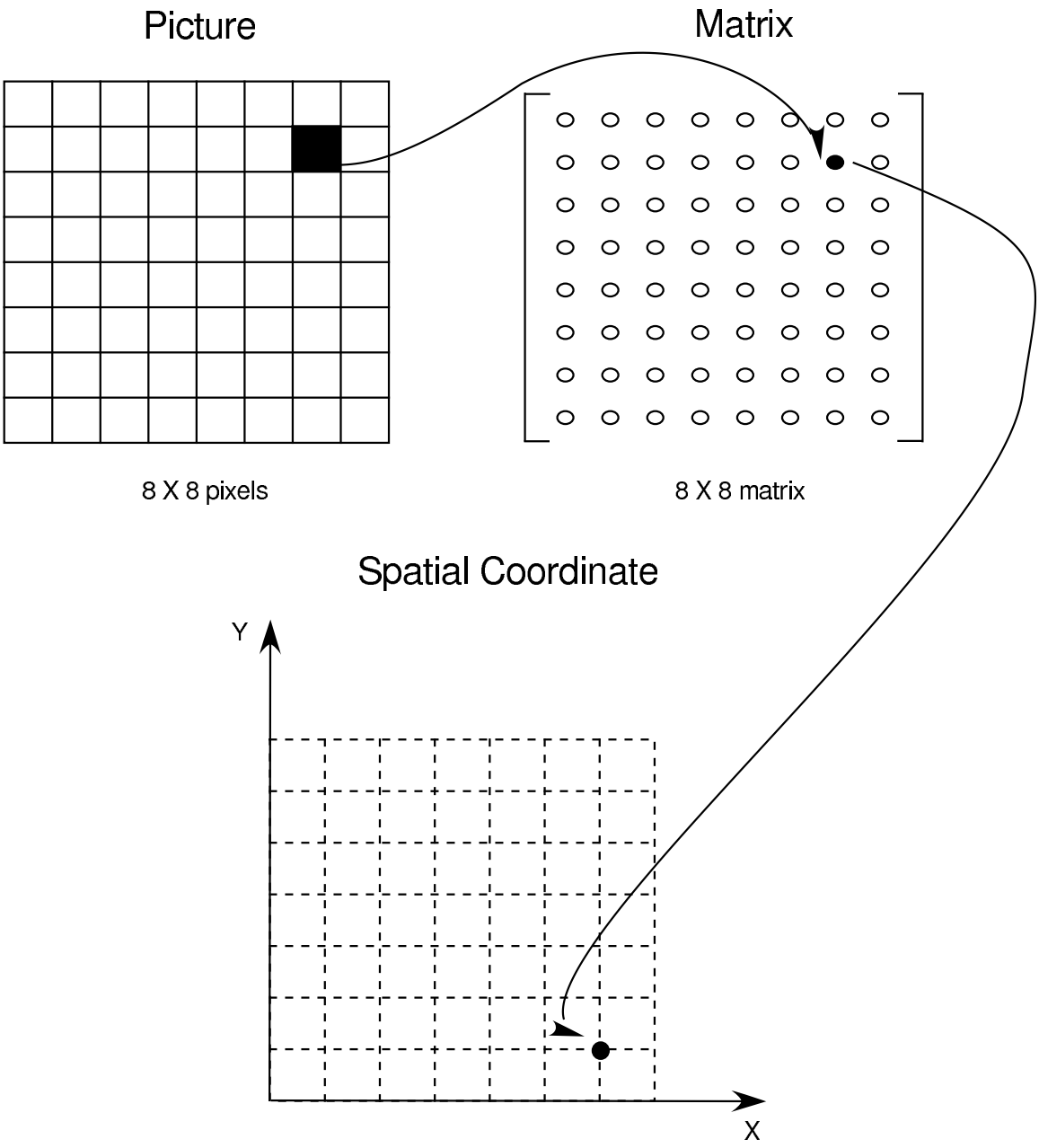

Figure 1.2: Conversions of Image to Matrix and Spatial Coordinates

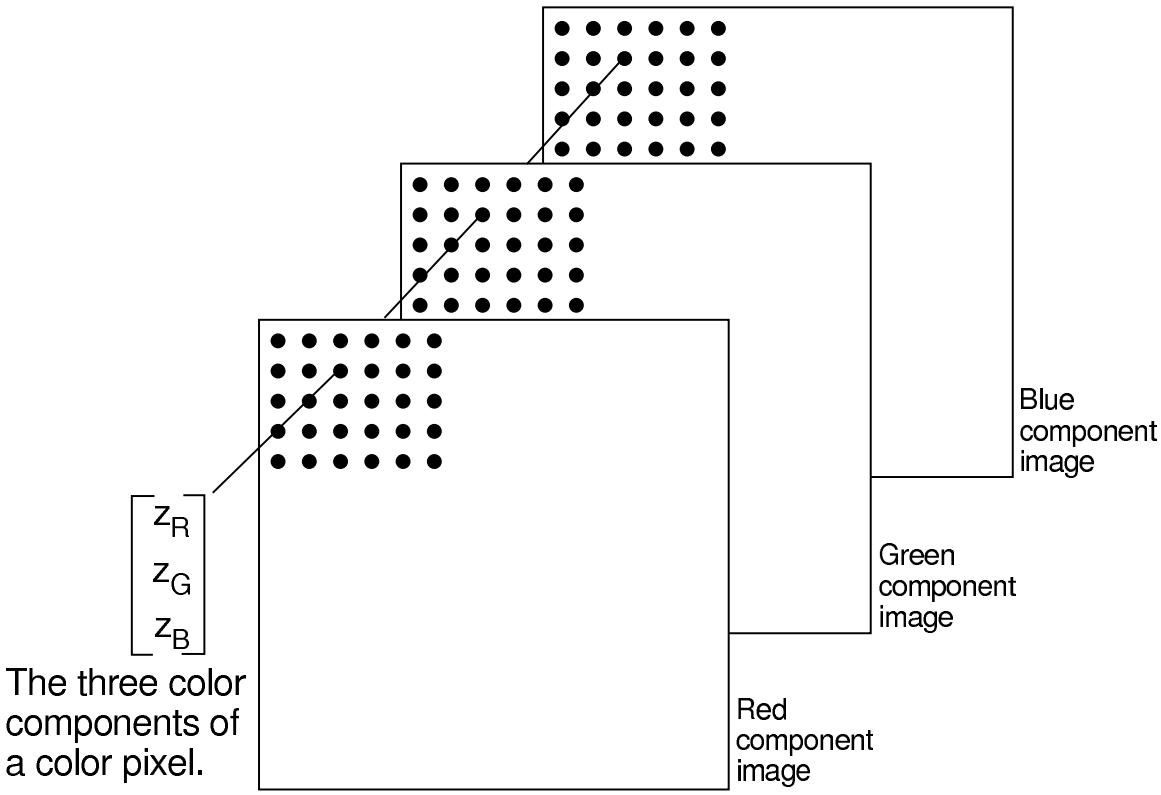

Figure 1.3: RGB Color Image

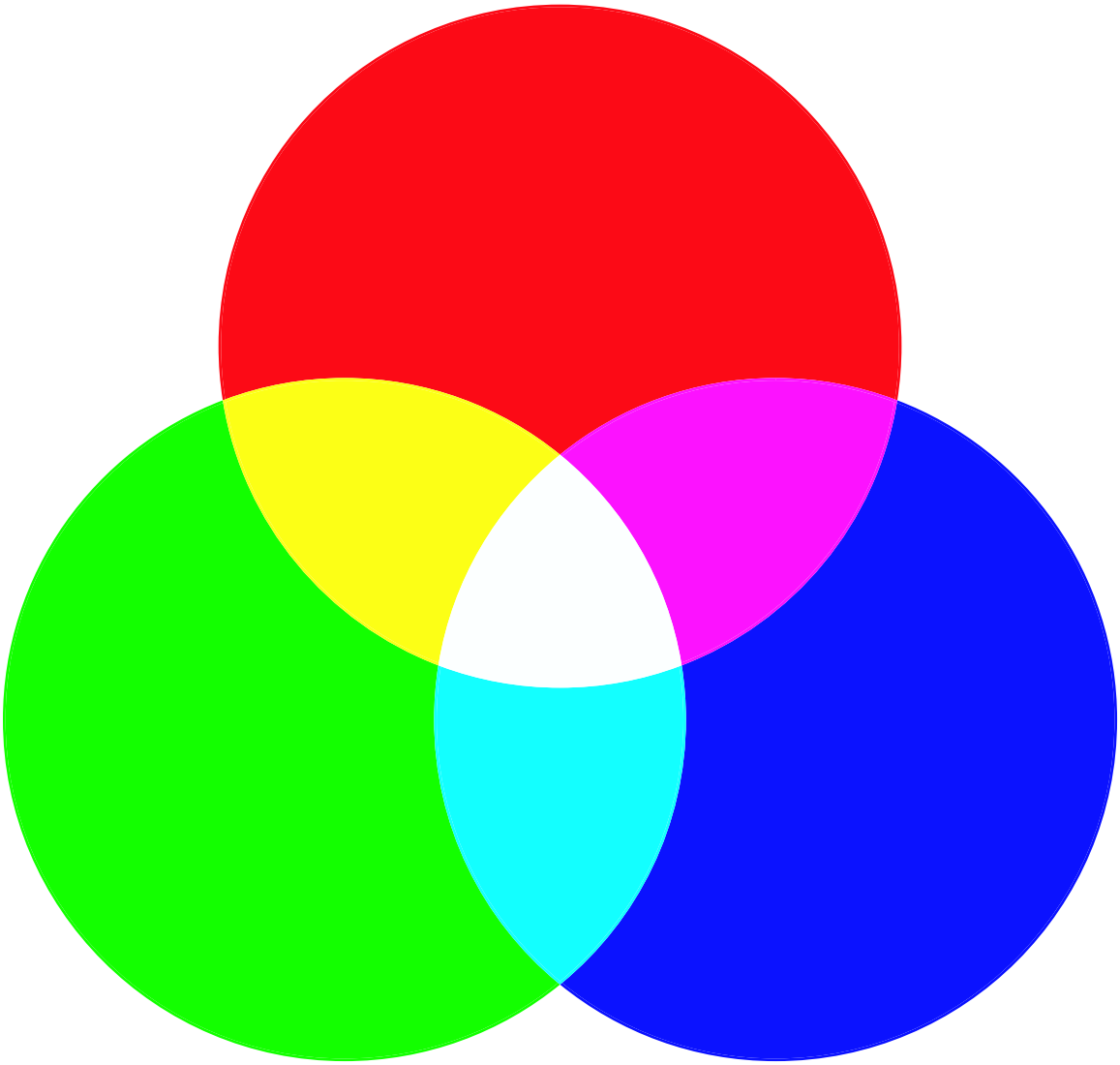

Figure 1.4: The Representation of Additive Color Mixing

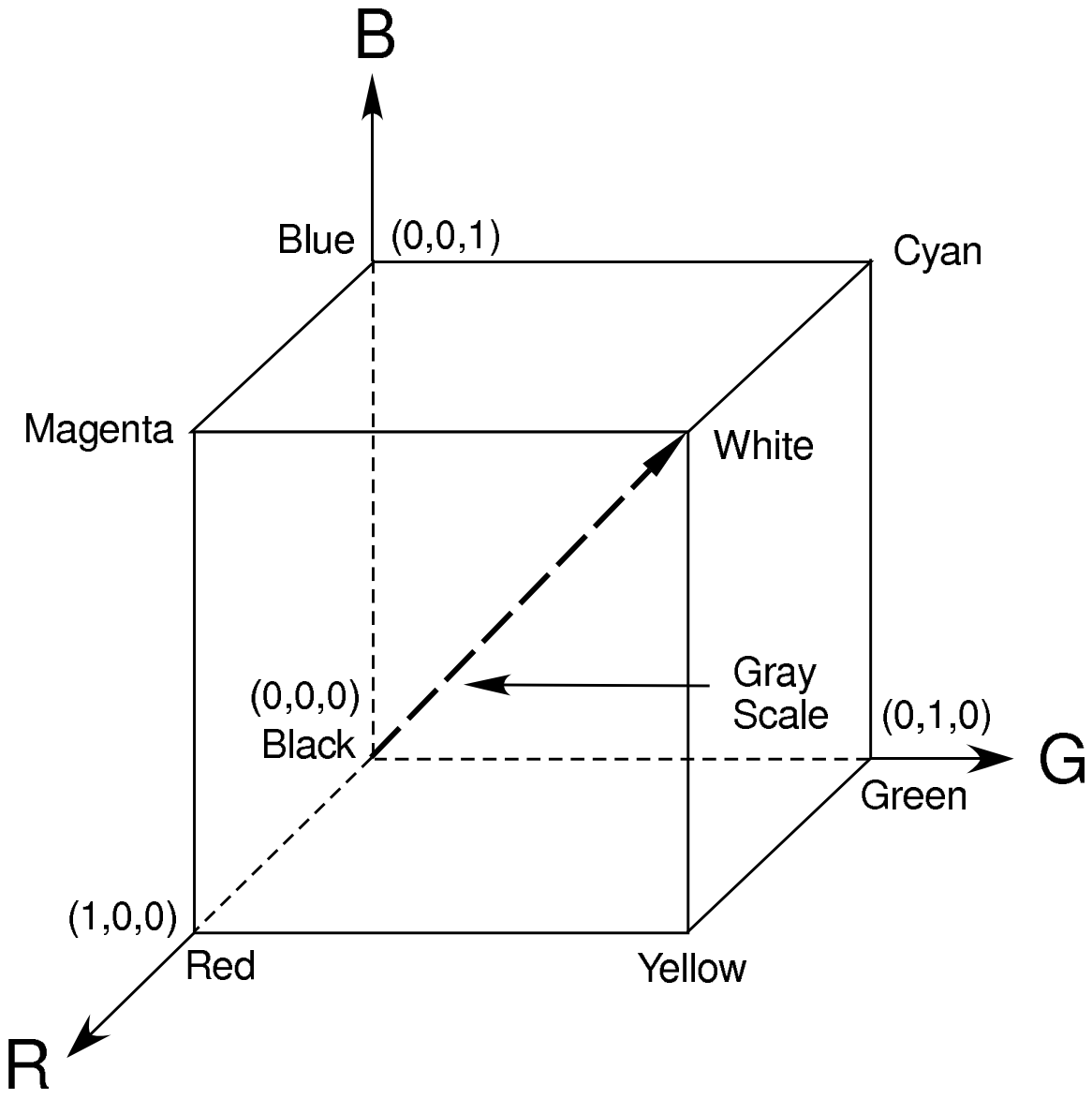

Figure 1.5: RGB Color Cube

data per pixel instead of 24-bit. As a result, the gray-scale image is an $M \times N \times 1$ matrix. In image processing, the input is often the intensity values at pixels and the output is the image itself.

In this thesis we will introduce some gray and color image denosing models and study their approximations by finite element methods. The main goals of this thesis are to present the state-of-the-art of these models and to numerically approximate them on computers.

1.2 Outline of the Thesis

The main question for image denosing is following one: Given a noisy/degraded image $g(x, y)$ which contains "unknown" additive noise $\eta(x, y)$, find the original image $u(x, y)$ such that

$$u(x, y) + \eta(x, y) = g(x, y). \tag{1.1}$$

In the case of gray images, g, η, and u are scalar-valued functions, while in the case of color images, g, η, and u are 3-component vector-valued functions. Problem (1.1) is an ill-posed inverse problem since its solutions are clearly not unique. To select the "best" physically meaningful solution, it is necessary to choose a selection criterion.

In Chapter 2, we deal with the total variation (TV) model which is the best known model for denoising gray images. The TV model was first introduced by Rudin, Osher and Fatemi [Rud92] in 1992. Edges in images are very important for understanding images. To accurately represent edges of images, Rudin, Osher and Fatemi postulated that image functions should be functions of the bounded total variation (BV) since BV functions can have jumps. Furthermore, they proposed that the "original" image u in (1.1) should be the BV function which has the least BV-norm (which measures

oscillations of BV funtions). The TV model has been used in many applications in image denoising, deblurring, and inpainting. In this chapter, we introduce the TV flow model and a regularized TV flow model, and survey uniqueness and existence results concerning these models. We also discuss the fully discrete finite element approximations of these models and survey error analysis and convergence results of the finite element approximations. Finally, we present some numerical simulations of the finite element schemes.

In Chapter 3, we address a related noise removal model for color images. As we describe above that a color image is expressed by a vectorial value $\mathbf{I}(x) = (r(x), g(x), b(x))$ for each pixel $x = (x_1, x_2)$ representing the intensity of three primary colors (Red, Green, Blue)

$$I : \Omega \subset \mathbf{R}^2 \to D := \{(R, G, B) : R, G, B \geq 0\} \subset \mathbf{R}^3.$$

Various approaches, such as the channel-by-channel, vector model denoising, and non-flat feature denoising for denoising color image have been introduced in the literature by many people. Some of these approaches directly treat the RGB color system as a vector space [Sap96, Blo98]. Most recent studies have proposed the use of the chromaticity and brightness(CB) model which is closer to human perception. The CB model basically decomposes $I(x)$ into two components, chromaticity and brightness. Chan *et al.* [Cha01] have verified that CB decomposition gives better denoised images than the channel-by-channel model which denoises each RGB channels separately. Another advantage of CB decomposition is that it allows one to denoise the chromaticity and the brightness separately by different methods. In this thesis, we use the TV model to denoise the brightness component and the p-harmonic map flow to denoise the chromaticity. Since the TV model is introduced in Chapter 2, we

only discuss the p-harmonic map flow in this chapter. Finite element approximations of the p-harmonic map flow and their error analysis are discussed. The numerical simulations are presented as well.

In Chapter 4, we present numerical simulations to compare the CB decomposition method and the channel-by-channel method for color image denoising. We then propose some generalizations of the p-harmonic model for denoising color images.

1.3 Programming

The finite element method, which is one of the best known numerical methods for solving PDEs, is used to approximate the PDEs of all noise removal models discussed in this thesis. For numerical tests, we use Matlab® and Comsol Multiphysics® software packages to do all simulations presented in this thesis.

Matlab® has an image processing toolbox, it produces a matrix (or array) which presents pixel values of an input image. It manipulates images like numbers. Also, it can save images in different formats such as gif, png, and jpg. It has a function to generate noise with different types and densities.

Comsol Multiphysics® is a popular software package for solving PDE problems by using the finite element method. It has a powerful GUI (graphical user interface) and is easy to create any domain and to generate meshes. Since an image consists of pixels which are tiny rectangles, we use rectangle meshes instead of triangle meshes in our simulations, which are also allowed in Comsol Multiphysics®. For each numerical simulation, we first generate the image dataset by Matlab®, then import the dataset into Comsol Multiphysics®. Each component of dataset is placed on a rectangle mesh

which corresponds to a pixel of the image. Next, we solve the PDE(s) of a selected image denoising model by Comsol Multiphysics®. Finally, we export computed solution from Comsol Multiphysics® into Matlab® to assemble the recovered image.

Chapter 2

Gray Image Denoising

In this chapter, we will consider gray image denosing and restoration. We will introduce the total variation denosing model of Rudin-Osher-Fatami [Rud92], the total variation flow, and finite element approximations of the total variation flow. Numerical tests and error analysis for the gray image model will be presented and summarized.

2.1 Introduction

Let $\tilde{u}$: $\Omega \subset \mathbf{R}^2 \to \mathbf{R}$ be a real gray level image without noise, and g: $\Omega \subset \mathbf{R}^2 \to \mathbf{R}$ be the same scene image with noise. Suppose that $u(x, y)$ and $g(x, y)$ denote the pixel values of the denoisied image and the noisy image at $(x, y) \in \Omega$, respectively. The total variation (TV) denosing model seeks the denoised image u as the function which minimizes the following functional

$$J(v) := \int_\Omega |\nabla v| \, dx \tag{2.1}$$

on $BV(\Omega)$, the space of functions of bounded total variation (defined below), subject to the constraints

$$\int_\Omega (v-g)\ dx\ dy = 0, \tag{2.2}$$

$$\int_\Omega \frac{1}{2}(v-g)^2\ dx\ dy = \sigma^2, \tag{2.3}$$

where $\sigma > 0$ is the error level and assumed to be known. The first constraint (2.2) corresponds to the assumption that the noise has zero-mean, and the second constraint (2.3) uses a *priori* information that the standard deviation of the noise $\eta(x,y) := u-g$ is σ [Cha97, Rud92].

We call that a function $u \in L^1(\Omega)$ is a function of *bounded variation* if all of its first order partial derivatives are measures with finite total variation in Ω. The gradient of such a function u, denoted by ∇u, is a vector-valued measure with the finite total variation

$$\int_\Omega |\nabla u|\ dx \equiv ||\nabla u|| := sup\left\{\int_\Omega -u \text{ div } \mathbf{v}\ dx\ ;\ \mathbf{v} \in [C_0^1(\Omega)]^N\ ,\ ||\mathbf{v}||_{L^\infty}\ \leq\ 1\right\}.$$

The space of functions with bounded total variations is defined as

$$BV(\Omega) = \{u : u \in L^1(\Omega) \text{ and } \int_\Omega |\nabla u|\ dx < \infty\},$$

it is a Banach space with the BV norm

$$||u||_{BV} := ||u||_{L^1} + ||\nabla u||,$$

and is continuously embedded in $L^1(\Omega)$ [Bar, Cha02].

To avoid solving the constrained minimization problem, the constrained TV model is often reformulated as an unconstrained problem by enforcing the constraints weakly. The unconstrained minimization problem reads as

$$\min J_\lambda(v) \tag{2.4}$$

where

$$J_\lambda(v) := \int_\Omega |\nabla v| \, dx + \frac{\lambda}{2} \int_\Omega |v - g|^2 \, dx, \tag{2.5}$$

and λ is a nonnegative penalization parameter that controls the trade-off between goodness of fit-to-the-data and variability in v.

The steepest descent method which is a well-known method for the unconstrained minimization problem, leads to consider its gradient flow:

$$\frac{\partial u}{\partial t} = \operatorname{div}\left(\frac{\nabla u}{|\nabla u|}\right) - \lambda(u - g) \qquad \text{in } \Omega_T \equiv \Omega \times (0, T), \tag{2.6}$$

$$\frac{\partial u}{\partial n} = 0 \qquad \text{on } \partial\Omega_T \equiv \partial\Omega \times (0, T), \tag{2.7}$$

$$u(\cdot, 0) = u_0(\cdot) \qquad \text{in } \Omega, \tag{2.8}$$

where T is a positive number and u_0 is an initial guess. In the rest of the thesis, we refer the above gradient flow as the TV flow. Many authors have addressed, analyzed, and approximated numerically the above TV flow. We refer to [Fen03] and the references therein for a detailed discussion about the TV flow and its numerical approximations. Chambolle and Lions [Cha97] presented existence and uniqueness result for

$$\min J(v) \tag{2.9}$$

subject to

$$\int_\Omega (v-g)\ dx\ dy = 0, \tag{2.10}$$

$$\int_\Omega \frac{1}{2}(v-g)^2\ dx\ dy = \sigma^2, \tag{2.11}$$

and proved that (2.9)-(2.11) is equivalent to the minimization of (2.5) for a unique and non-negative λ under the specific assumptions. We refer to [Cha97] for a more detailed discussion.

To avoid dividing by zero in numerical simulations, we regularize $|\nabla u|$ by $\sqrt{|\nabla u|^2+\varepsilon^2}$ for $\varepsilon > 0$. This is a well-known regularization technique to approximate and compute the minimizer of the total variation energy and its variants [Fen03]. We compute the solution of the following regularized problem

$$\frac{\partial u^\varepsilon}{\partial t} = \operatorname{div}\left(\frac{\nabla u^\varepsilon}{\sqrt{|\nabla u^\varepsilon|^2+\varepsilon^2}}\right) - \lambda(u^\varepsilon - g) \qquad \text{in } \Omega_T, \tag{2.12}$$

$$\frac{\partial u^\varepsilon}{\partial n} = 0 \qquad \text{on } \partial\Omega_T, \tag{2.13}$$

$$u^\varepsilon(\cdot,0) = u_0(\cdot) \qquad \text{in } \Omega. \tag{2.14}$$

The energy functional corresponding to the equation (2.12) is

$$J_{\lambda,\varepsilon}(v) := \int_\Omega \sqrt{|\nabla v|^2+\varepsilon^2}\ dx + \frac{\lambda}{2}\int_\Omega |v-g|^2\ dx, \tag{2.15}$$

which is a convex regularization to the total variation functional (2.5).

The remainder of this chapter is organized as follows. In Section 2.2, we summarize existence and uniqueness results for the regularized flow and the TV flow. In Section 2.3, we discuss finite element approximations, error analysis and convergence rate for

the TV flow. In Section 2.4, we present some numerical simulations for gray image denoising via (2.12)-(2.14).

2.2 The Total Variation Denoising Model

In this section, we summarize existence and uniqueness results for the gradient flow (2.12)-(2.14) and the TV flow (2.6)-(2.8).

Remark 2.1. *Since images are defined in rectangles, hence* $\Omega \subset \mathbf{R}^2$ *for the image processing applications. Mathematically, existence and uniqueness theorems of solutions for the gradient flow (2.12)-(2.14) and the TV flow (2.6)-(2.8) holds for* $\Omega \subset \mathbf{R}^N$ *(*$N \geq 2$*). Thus, all theorems will be stated for* $\Omega \subset \mathbf{R}^N$ *(*$N \geq 2$*).*

The first theorem, which was proved in [Fen03], states existence and uniqueness for the gradient flow (2.12)-(2.14) in the spirit of [Lic78,Ger80] for the minimal surface and the prescribed mean curvature flow, respectively.

Theorem 2.1. *Let* $\Omega \subset \boldsymbol{R}^N (N \geq 2)$ *be a bounded domain with Lipschitz boundary* $\partial\Omega$*. Suppose that* $u_0, g \in L^2(\Omega)$*. Then, there exists a unique function* $u^\varepsilon \in L^1((0,T);\, BV(\Omega)) \bigcap C^0([0,T];\, L^2(\Omega))$ *such that*

$$u^\varepsilon(0) = u_0, \qquad\qquad u_t^\varepsilon \in L^2((0,T);\, H^{-1}(\Omega)), \tag{2.16}$$

and for any $s \in [0,T]$

$$\begin{aligned} &\int_0^s \int_\Omega v_t(v-u^\varepsilon)\,dx\,dt + \int_0^s [J_{\lambda,\varepsilon}(v) - J_{\lambda,\varepsilon}(u^\varepsilon)]\,dt \\ &\qquad \geq \frac{1}{2}\Big[\|v(s)-u^\varepsilon(s)\|_{L^2}^2 - \|v(0)-u_0\|_{L^2}^2\Big] \\ &\qquad \forall\, v \in L^1((0,T);\, BV(\Omega)) \cap L^2(\Omega_T) \text{ such that } v_t \in L^2(\Omega_T). \end{aligned} \tag{2.17}$$

Moreover, suppose $u_i^\varepsilon\,(i=1,2)$ *are two functions which satisfy (2.17) with respective datum functions* $u_i^\varepsilon(0), g_i^\varepsilon\,(i=1,2)$. *Then, there holds*

$$\|u_1^\varepsilon - u_2^\varepsilon\|_{L^2} \le \|u_1^\varepsilon(0) - u_2^\varepsilon(0)\|_{L^2} + \sqrt{\lambda}\,\|g_1^\varepsilon - g_2^\varepsilon\|_{L^2} \qquad \forall\, s \in [0,T]. \tag{2.18}$$

We remark that we shall define a weak solution of the gradient flow (2.12)-(2.14) as a function $u^\varepsilon \in L^1\left((0,T);\, BV(\Omega)\right) \cap C^0\left([0,T];\, L^2\left(\Omega\right)\right)$ which satisfies (2.16)-(2.17) by applying the idea of [Lic78, Ger80]. Also, Theorem 2.1 can be easily generalized to the cases of nonhomogeneous Dirichlet and Neumann boundary conditions following [Lic78, Ger80], under some appropriate assumptions on the boundary data. For example, consider the nonhomogeneous Dirichlet boundary condition case

$$u^\varepsilon = \phi \qquad \text{on } \partial\Omega \times (0,T),$$

we only need to replace the energy functional $J_{\lambda,\varepsilon}(\cdot)$ by the energy functional

$$\Phi_{\lambda,\varepsilon}(u) := J_{\lambda,\varepsilon}(u) + \int_{\partial\Omega} |u-\phi|\, dx, \tag{2.19}$$

where the Dirichlet datum is enforced weakly (see [Lic78, Ger80, Giu84] for more discussions). Then, all results of Theorem 2.1 can be extended to this case under some suitable assumptions on ϕ, and particularly the analysis remains same (*cf.* [Fen03]).

Our second theorem [Fen03] addresses existence and uniqueness of solutions for the TV flow; it also shows that the TV flow is the limiting problem of the gradient flow (2.12)-(2.14) as $\varepsilon \to 0$

Theorem 2.2. *Let* $\Omega \subset \boldsymbol{R}^N (N \ge 2)$ *be a bounded domain with Lipschitz boundary* $\partial\Omega$ *and* $u_0,\, g \in L^2(\Omega)$.

(i) There exists a unique function $u \in L^1((0,T);\, BV(\Omega)) \cap C^0([0,T];\, L^2(\Omega))$ *such that*

$$u(0) = u_0, \qquad u_t \in L^2((0,T);\, H^{-1}(\Omega)), \tag{2.20}$$

and for any $s \in [0,T]$

$$\begin{aligned} &\int_0^s \int_\Omega v_t(v-u)\,dx\,dt + \int_0^s [J_\lambda(v) - J_\lambda(u)]\,dt \\ &\qquad \geq \frac{1}{2}\Big[\|v(s)-u(s)\|_{L^2}^2 - \|v(0)-u_0\|_{L^2}^2\Big] \\ &\qquad \forall\, v \in L^1((0,T);\, BV(\Omega)) \cap L^2(\Omega_T) \text{ such that } v_t \in L^2(\Omega_T). \end{aligned} \tag{2.21}$$

(ii) Suppose $u_i\,(i=1,2)$ *are two functions which satisfy (2.21) with respective datum functions* $u_i(0), g_i\,(i=1,2)$*. Then,*

$$\|u_1 - u_2\|_{L^2} \leq \|u_1(0) - u_2(0)\|_{L^2} + \sqrt{\lambda}\,\|g_1 - g_2\|_{L^2} \qquad \forall\, s \in [0,T]. \tag{2.22}$$

(iii) Let u^ε *be the weak solution of the gradient flow (2.12)-(2.14) as stated in Theorem 2.1, then there holds*

$$\begin{aligned} &\lim_{\varepsilon\to 0} \|u^\varepsilon(t) - u(t)\|_{L^p(\Omega)} = 0 \text{ for a.e. } t \in (0,T),\ \forall\, p \in \Big[1, \frac{N}{N-1}\Big), \\ &u_t^\varepsilon \to u_t \quad \text{weakly in } L^2((0,T);\, H^{-1}(\Omega)). \end{aligned} \tag{2.23}$$

Similarly, a weak solution of the TV flow (2.6)-(2.8) will be defined as a function $u \in L^1((0,T);\, BV(\Omega))$ which satisfies (2.20)-(2.21) with the same reason as stated for Theorem 2.1. It is clear that this definition comes naturally in view of Theorem 2.1 and the convergence result (2.23) [Fen03]. In the context of image processing, $\partial\Omega$ is usually piecewise smooth and the observed image $g \in L^\infty$, although the initial

condition is less restrictive. As a result, we can only expect weak solution for the gradient flow (2.12)-(2.14).

The following theorem [Fen05] shows convergence rate of the regularization procedure in power of ε.

Theorem 2.3. *Suppose that u_0^ε, $g \in L^2(\Omega)$. Let u^ε, u be the weak solution of (2.12)-(2.14) and (2.6)-(2.8), respectively, there exists a positive constant $C_0 = C_0(T)$ such that*

$$\operatorname*{ess\,sup}_{t\in[0,T]} \|u(t) - u^\varepsilon(t)\|_{L^2(\Omega)} \leq \|u_0 - u_0^\varepsilon\|_{L^2(\Omega)} + 2\sqrt{C_0(T)}\,\varepsilon^{\frac{1}{2}}. \tag{2.24}$$

2.3 Finite Element Approximations for the Total Variation Flow

In this section, we describe the finite element method for the TV flow and summarize error analysis results for the finite element method.

Remark 2.2. *For practical reasons, we let $N = 2$ throughout this subsection although the results cited below also hold in the case $N = 3$.*

Remark 2.3. *We will consistently omit writing dx after integrals over domains and ds after integrals over $\partial\Omega$ since it is understood that we are integrating with respect to the variables on which the domain is defined.*

Our main goal is to construct computable approximate solutions for the solution u of the gradient flow (2.12)-(2.14), where $\Omega \subset \mathbf{R}^2$ is a bounded open domain with Lipschitz boundary $\partial\Omega$ and

$$V := H^1(\Omega) = \{v :\ v \in L^2(\Omega),\, \nabla v \in\ [L^2(\Omega)]^2\}.$$

We will first derive the variational formulation for (2.12)-(2.14), and then proceed to formulate a semi-discrete finite element approximation and a fully discrete finite element approximations.

2.3.1 Variational Formulation

Let

$$f_\varepsilon(z) = \sqrt{z^2 + \varepsilon^2},$$

then

$$\frac{|\nabla u^\varepsilon|}{\sqrt{|\nabla u^\varepsilon|^2 + \varepsilon^2}} = f'_\varepsilon(|\nabla u^\varepsilon|).$$

To derive the variational formulation, for a fixed $t \in (0, T)$ multiply both sides of (2.12) by a test function $v \in V$, then integrate over Ω:

$$\int_\Omega \Big\{ \frac{\partial u^\varepsilon}{\partial t}\, v - \operatorname{div}\left(\frac{f'_\varepsilon(|\nabla u^\varepsilon|)\, \nabla u^\varepsilon}{|\nabla u^\varepsilon|} \right) v + \lambda\, u^\varepsilon\, v \Big\} = \int_\Omega \lambda\, g\, v. \tag{2.25}$$

Using Green's formula on the left hand side of (2.25) we get

$$\int_\Omega \Big(\frac{\partial u^\varepsilon}{\partial t}\, v + \frac{f'_\varepsilon(|\nabla u^\varepsilon|)}{|\nabla u^\varepsilon|}\, \nabla u^\varepsilon \cdot \nabla v + \lambda\, u^\varepsilon\, v \Big) - \int_{\partial\Omega} \frac{f'_\varepsilon(|\nabla u^\varepsilon|)}{|\nabla u^\varepsilon|}\, \frac{\partial u^\varepsilon}{\partial n}\, v = \int_\Omega \lambda\, g\, v, \tag{2.26}$$

where ∇ denotes the gradient operator. By the boundary condition (2.13), the second integral on the left-hand side of (2.26) vanishes. Hence,

$$\int_\Omega \Big(\frac{\partial u^\varepsilon}{\partial t}\, v + \frac{f'_\varepsilon(|\nabla u^\varepsilon|)}{|\nabla u^\varepsilon|}\, \nabla u^\varepsilon \cdot \nabla v + \lambda\, u^\varepsilon\, v \Big) = \int_\Omega \lambda\, g\, v. \tag{2.27}$$

We now define the weak formulation for (2.12)-(2.14) as follows: Find $u^\varepsilon \in L^2((0,T);\, V) \cap H^1((0,T);\, L^2(\Omega))$ such that

$$(u_t^\varepsilon, v) + a(u^\varepsilon, v) + \lambda\, b(u^\varepsilon, v) = \lambda\,(g, v) \qquad \forall\, v \in V, \tag{2.28}$$

$$(u^\varepsilon(\cdot, 0), v) = (u_0(\cdot), v) \qquad \forall\, v \in V, \tag{2.29}$$

where

$$\begin{aligned}
(u_t^\varepsilon, v) &= \int_\Omega \frac{\partial u^\varepsilon}{\partial t}\, v, \\
a(u^\varepsilon, v) &= \int_\Omega \frac{f_\varepsilon'(|\nabla u^\varepsilon|)}{|\nabla u^\varepsilon|}\, \nabla u^\varepsilon \cdot \nabla v, \\
b(u^\varepsilon, v) &= \int_\Omega u^\varepsilon\, v, \\
(g, v) &= \int_\Omega g\, v.
\end{aligned}$$

We now construct a finite-dimensional subspace V_h of V. Let $\mathcal{T}_h = \{K_1, \ldots, K_{m_R}\}$ be a quasi-uniform triangulation of $\Omega \subset \mathbf{R}^2$ with mesh size $h \in (0,1)$ and $\overline{\Omega} = \bigcup\limits_{K \in \mathcal{T}_h} \overline{K}$, so that all elements K of $\mathcal{T}_h$ roughly have the same size. Here K_i are non-overlapping triangles.

Remark 2.4. *When $N = 3$, K_i are not triangles, they are tetrahedrons instead.*

Next, we define V_h to be the finite element space of continuous, piecewise linear functions associated with T_h, that is,

$$V_h := \{v_h :\, v_h \in C^0(\overline{\Omega}),\, v_h|_K \in P_1(K),\, \forall\, K \in \mathcal{T}_h\},$$

where $v_h|_K$ denotes the restriction of v to K, and $P_1(K)$ stands for the set of all linear polynomials on K.

Remark 2.5. *We could define the finite element space of continuous, piecewise polynomials of degree less than or equal to r on K for any positive integer r, however, for presentation clarity, we confine ourself to the case $r = 1$ in this thesis.*

2.3.2 Semi-Discrete Finite Element Approximation

Let $\mathcal{N}_h := \{p_i\}$, $(i = 1, \ldots, m_x,)$ be a set of all vertices of the triangulation $\mathcal{T}_h$. Every function $v \in V_h$ is uniquely determined by its nodal values $\eta_j = v(p_j)$, $j = 1, \cdots, m_x$. Let $\varphi_j \in V_h$ be a piecewise linear function corresponding such that

$$\varphi_j(p_i) = \delta_{ij} \equiv \begin{cases} 1 & \text{if } i = j, \\ 0 & \text{if } i \neq j \end{cases} \qquad i,\ j = 1, \ldots, m_x.$$

It is easy to check that each φ_j is uniquely determined and the set $\{\varphi_j\}$ forms a basis for V_h. The support of each basis function (the closure of the set of points for which $\varphi_j(x) \neq 0$) consists of the triangles with the common vertex p_i.

With these basis functions of the finite element subspace V_h in place, we can represent any $v_h \in V_h$ as

$$v_h(x) = \sum_{j=1}^{m} \eta_j \, \varphi_j(x) \qquad \forall\, x \in \overline{\Omega}, \tag{2.30}$$

where $\eta_j = v_h(p_j)$, $j = 1, \cdots, m_x$. The semi-discrete finite element method for (2.28)-(2.29) is now defined as: Find $u_h : [0, T] \to V_h$ such that

$$(\dot{u}_h^\varepsilon, v_h) + a(u_h^\varepsilon, v_h) + \lambda\, b(u_h^\varepsilon, v_h) = \lambda\, (g, v_h) \qquad \forall\, v_h \in V_h, \tag{2.31}$$

$$(u_h^\varepsilon(\cdot, 0), v_h) = (u_0(\cdot), v_h) \qquad \forall\, v_h \in V_h. \tag{2.32}$$

Remark 2.6. *To avoid inconvenient subscripts, $\dot{u}_h$ will be used to denote the time derivative* $\dfrac{\partial u_h}{\partial t}$.

Since $u_h^\varepsilon \in V_h$ we can express u_h^ε in terms of the basis functions $\{\varphi_i\}_{i=1}^{m_x}$ of V_h as follows:

$$u_h^\varepsilon(x,t) = \sum_{i=1}^{m_x} \xi_i(t)\,\varphi_i(x) \qquad (x,t) \in \Omega \times (0,T), \tag{2.33}$$

where $\xi_i(t) = u_h(p_i,t)$. Substituting (2.33) and $v_h = \varphi_j$ in (2.31)-(2.32), we get

$$\begin{aligned} \sum_{i=1}^{m_x} \dot{\xi}_i^\varepsilon(t)(\varphi_i(x),\varphi_j(x)) + \sum_{i=1}^{m_x} \xi_i^\varepsilon(t)\hat{a}(\varphi_i(x),\varphi_j(x)) + \lambda \sum_{i=1}^{m_x} \xi_i^\varepsilon(t)(\varphi_i(x),\varphi_j(x)) \\ = \lambda(g,\varphi_j) \quad j = 1,\ldots,m_x, \qquad t \in (0,T), \end{aligned} \tag{2.34}$$

$$\sum_{i=1}^{m} \xi_i^\varepsilon(0)(\varphi_i(x),\varphi_j(x)) = (u_0,\varphi_j) \qquad j = 1,\ldots,m_x, \tag{2.35}$$

where

$$\hat{a}(\varphi_i(x),\varphi_j(x)) = \int_\Omega \frac{f_\varepsilon'(|\sum_{i=1}^{m_x} \xi_i^\varepsilon(t)\nabla\varphi_i(x)|)}{|\sum_{i=1}^{m_x} \xi_i^\varepsilon(t)\nabla\varphi_i(x)|}\,\nabla\varphi_i(x)\cdot\nabla\varphi_j(x).$$

In matrix notation (2.34)-(2.35) can be written as

$$L\dot{\xi}^\varepsilon(t) + (\hat{A} + \lambda\, L)\xi^\varepsilon(t) = \lambda c \qquad \forall\, t \in (0,T), \tag{2.36}$$

$$L\xi^\varepsilon(0) = \chi, \tag{2.37}$$

where

$$L = [L_{ij}], \qquad L_{ij} := (\varphi_i, \varphi_j), \tag{2.38}$$

$$\hat{A} = [\hat{A}_{ij}(\xi^\varepsilon(t))], \qquad \hat{A}_{ij}(\xi(^\varepsilon t)) := \hat{a}(\varphi_i, \varphi_j), \tag{2.39}$$

$$c = (c_1, \cdots, c_{m_x})^T, \qquad c_j := (g, \varphi_j), \tag{2.40}$$

$$\chi = (\chi_1, \cdots, \chi_{m_x})^T, \qquad \chi_j := (u_0, \varphi_j). \tag{2.41}$$

Equations (2.36)-(2.37) form a nonlinear ODE system in $\xi^\varepsilon(t)$.

2.3.3 Fully Discrete Finite Element Approximation

In order to discretize in time, we introduce (uniform) partition of the interval $[0, T]$. Let $\{t_n\}_{n=0}^{m_T}$ be an equally spaced partition of $[0, T]$ of mesh size $k = t_n - t_{n-1} \in (0, 1),\ n = 1, \ldots, m_T$ and introduce the notation $d_t U^n := \dfrac{u^n - u^{n-1}}{k}$. Then the fully discrete finite element discretization of the gradient flow (2.12)-(2.14) is defined as follows: Find $U^n \in V_h$ for $n = 1, \ldots, m_T$ such that

$$(d_t U^n, v_h) + \hat{a}(U^n, v_h) + \lambda\, b(U^n, v_h) = \lambda(g, v_h) \qquad \forall\, v_h \in V_h, \tag{2.42}$$

$$U^0(\cdot) = u_h^\varepsilon(\cdot, 0) \qquad \forall\, v_h \in V_h, \tag{2.43}$$

where

$$(d_t U^n, v_h) = \int_\Omega d_t U^n\, v_h, \tag{2.44}$$

$$\hat{a}(U^n, v_h) = \int_\Omega \frac{f_\varepsilon'(|\nabla U^n|)}{|\nabla U^n|}\, \nabla U^n\, \nabla v_h, \tag{2.45}$$

$$b(U^n, v_h) = \int_\Omega U^n\, v_h, \tag{2.46}$$

$$(g, v_h) = \int_\Omega g\, v_h. \tag{2.47}$$

Remark 2.7. *The above scheme is the implicit Euler method for (2.36)-(2.37).*

It is easy to see that (2.42) can be rewritten as the following system of equations:

$$\begin{aligned}(L + k(\hat{A}(\xi^n) + \lambda\, L))\xi^n &= L\xi^{n-1} + k\lambda b \qquad n = 1, \ldots, m_T,\\ \xi^0 &= \xi^\varepsilon(0) = L^{-1}\chi,\end{aligned}$$

where ξ^n is an approximation to $\xi(t_n)$.

As we can see that (2.45) is well-defined for all values of $|\nabla U^n|$ for $f'_\varepsilon(z) = \dfrac{z}{\sqrt{z^2+\varepsilon^2}}$. Since $f_\varepsilon(z)$ is strictly convex, it can be shown that (2.42)-(2.43) has a unique solution $\{U^n\}$. In fact, it also can be verified that the finite element scheme (2.42) satisfies the following stability estimate [Fen03]:

$$\|U_1^n - U_2^n\|_{L^2} \le \|U_1^0 - U_2^0\|_{L^2} + \sqrt{\lambda}\|g_1 - g_2\|_{L^2} \qquad 0 \le n \le m_T, \tag{2.48}$$

where U_i^n, $(i = 1, 2)$ is the solution of (2.42) with initial data U_i^0, g_i $(i = 1, 2)$, respectively. As we have shown, the fully discrete finite element scheme is based on the weak formulation of (2.28)-(2.29). To derive error analysis of the fully discrete finite element scheme, it requires some regularity of the solution u^ε, which asks for some regularity of u_0 and g. One way to get the regularity of u_0 and g is first to smoother the datum functions u_0 and g, denote the regularized functions by $\hat{u}_0$ and $\hat{g}$, respectively, then to work with the same differential equation with the new data $\hat{u}_0$ and $\hat{g}$. By the stability estimate (2.18), this approach is possible [Fen03].

For the fully discrete finite element solution U^n, we define its constant and linear interpolations in t as follows:

$$\overline{U}^{\varepsilon,h,k}(\cdot,t) := U^{n-1}(\cdot) \qquad \forall\, t \in [t_{n-1}, t_n), \quad 1 \le n \le m_T,$$
$$\overline{\overline{U}}^{\varepsilon,h,k}(\cdot,t) := \frac{t-t_{n-1}}{k}U^n(\cdot) + \frac{t_{n-1}-t}{k}U^{n-1}(\cdot) \qquad \forall\, t \in [t_{n-1}, t_n], \quad 1 \le n \le m_T.$$

Clearly, $\overline{U}^{\varepsilon,h,k}$ is continuous in x but discontinuous in t. On the other hand $\overline{\overline{U}}^{\varepsilon,h,k}$ is continuous in both x and t. The next two theorems [Fen03] give an error analysis for the above fully discrete finite element approximation.

Theorem 2.4. *Suppose that $u_0 \in H^1_{\rm loc}(\Omega) \cap W^{1,1}(\Omega)$, $g \in L^2(\Omega) \cap H^1_{\rm loc}(\Omega)$ and $\partial\Omega \in C^2$, then the solution u^ε of the gradient flow (2.12)-(2.14) belongs to $L^\infty((0,T);$ $W^{1,1}(\Omega)) \cap L^\infty((0,T);\, H^1_{\rm loc}(\Omega))$. Then, for each fixed $\varepsilon > 0$, U^n satisfies*

$$k\sum_{m=1}^{l}\left[\|d_t U^m\|^2_{L^2} + \frac{\lambda k}{2}\|d_t(U^m - g)\|^2_{L^2}\right] + J_{0,\varepsilon}(U^l) \le J_{0,\varepsilon}(U^0), \qquad 1 \le l \le m_T.$$

Moreover, under the following starting value constraint:

$$\lim_{h\to 0}\|u_0 - U^0\|_{L^2} = 0,$$

there also hold

$$\lim_{h,\,k\to 0}\|u^\varepsilon - \overline{U}^{\varepsilon,\,h,\,k}\|_{L^\infty((0,T);\,L^p(\Omega))} = 0, \tag{2.49}$$
$$\lim_{h,\,k\to 0}\|u^\varepsilon - \overline{\overline{U}}^{\varepsilon,\,h,\,k}\|_{L^\infty((0,T);\,L^p(\Omega))} = 0, \tag{2.50}$$

uniformly in ε for any $p \in [1, \dfrac{N}{N-1})$ and $N = 1, 2, 3$.

Theorem 2.5. *Let u stand for the weak solution of the TV flow (2.6)-(2.8). Under assumptions of Theorem 2.4 there hold*

$$\lim_{\varepsilon\to 0}\lim_{h,\,k\to 0}\|u-\overline{U}^{\varepsilon,\,h,\,k}\|_{L^\infty((0,T);\,L^p(\Omega))} = 0, \tag{2.51}$$

$$\lim_{\varepsilon\to 0}\lim_{h,\,k\to 0}\|u-\overline{\overline{U}}^{\varepsilon,\,h,\,k}\|_{L^\infty((0,T);\,L^p(\Omega))} = 0, \tag{2.52}$$

for any $p\in[1,\dfrac{N}{N-1})$ *and* $N=1,2,3$.

Our last theorem [Fen05] provides a rate of convergence for the error $u-\overline{\overline{U}}^{\varepsilon,\,h,\,k}$.

Theorem 2.6. *Suppose that* $u_0\in C^2(\overline{\Omega})$, $g\in L^\infty((0,T);\,W^{1,\infty}(\Omega))$, $\partial\Omega\in C^3$. *Then, under the following starting value and mesh constraints*

$$\|u_0^\varepsilon-U^0\|_{L^2}\le Ch^2 \ \ \textit{and} \ \ k=\mathrm{O}\,(h^2),$$

there holds the error estimate

$$\operatorname*{ess\,sup}_{t\in\,[0,T]}\|u-\overline{\overline{U}}^{\varepsilon,\,h,\,k}\|_{L^2(\Omega)}\le C_1(\varepsilon)k+C_2(\varepsilon)h^2+2\sqrt{|\Omega|T}\,\sqrt{\varepsilon},$$

where $C_i(\varepsilon)$ *for* $i=1,2$ *are positive constants which depend on* ε^{-1} *in some low polynomial order.*

2.4 Numerical Tests

In this section, we provide some numerical tests for the TV flow. In each test, we add a Gaussian noise with variance 0.2 to the original test image to get a noisy image g. We then use the TV model with the fully discrete finite element method to remove the noise and to get a denoised image u which should be very close to the original

image. We use the peak-signal-to-noise ratio (PSNR) measured in dB to measure the quality of denoised images. To compute PSNR, we need to compute the mean squared error (MSE) of the reconstructed image which is defined by

$$MSE(u-g) = E(u-g)^2 = \sum \frac{(u-g)^2}{(\text{size of image})^2}.$$

Then, the PSNR is given by

$$PSNR = 10 \log_{10} \Big(\frac{MAX^2}{MSE} \Big),$$

where MAX is the maximum pixel value, e.g., 255 for 8 bit images [Bov05]. The PSNR is relative measure, that is, the comparison between two values for different denoised images gives the measure of quality. An image with a higher PSNR value has a better quality than an image of the same scene but with a lower PSNR value does. $\lambda = 100$ and the time step $k = 1E-5$ are used for the numerical tests. Figure 2.1 is an original cameraman image and Figure 2.2 is a noisy cameraman image with Gaussian noise added in Figure 2.1. Figure 2.3-Figure 2.6 show the snapshots of TV flow of Figure 2.2. It is easy to see that noise in Figure 2.2 is gradually removed as t gets larger. Figures 2.7 and 2.8 are an original pepper image and a noisy pepper image, respectively. Also, snapshots of TV flow of Figure 2.8 are provided from Figure 2.9-Figure 2.12. Another numerical test is shown in Figure 2.13 which is an original mandril image. Like other tests, a noisy mandril image with Gaussian noise with zero mean and 0.2 variance can be seen in Figure 2.14 and the snapshots of TV flow of Figure 2.14 are presented in Figure 2.15-Figure 2.18. According to the numerical results, edges in denoised images smear when t gets too large.

Figure 2.1: Original Cameraman Image

Figure 2.2: Snapshot of TV Flow at $t = 0$ with $h = 2E - 3$, PSNR=42.82

Figure 2.3: Snapshot of TV Flow at $t = 5E - 5$ with $h = 2E - 3$, PSNR=67.42

Figure 2.4: Snapshot of TV Flow at $t = 1E-4$ with $h = 2E-3$, PSNR=61.19

Figure 2.5: Snapshot of TV Flow at $t = 1.5E-4$ with $h = 2E-3$, PSNR=55.58

Figure 2.6: Snapshot of TV Flow at $t = 2E-4$ with $h = 2E-3$, PSNR=51.41

Figure 2.7: Original Pepper Image

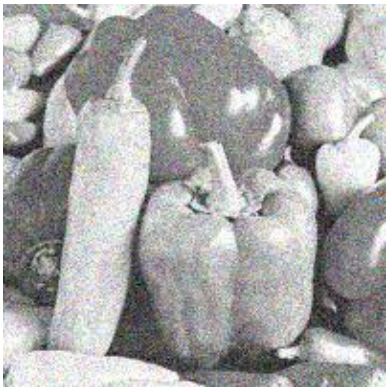

Figure 2.8: Snapshot of TV Flow at $t = 0$ with $h = 5E - 3$, PSNR=54.30

Figure 2.9: Snapshot of TV Flow at $t = 5E - 5$ with $h = 5E - 3$, PSNR=65.57

Figure 2.10: Snapshot of TV Flow at $t = 1E-4$ with $h = 5E-3$, PSNR=66.04

Figure 2.11: Snapshot of TV Flow at $t = 1.5E-4$ with $h = 5E-3$, PSNR=65.85

Figure 2.12: Snapshot of TV Flow at $t = 2E-4$ with $h = 5E-3$, PSNR=62.75

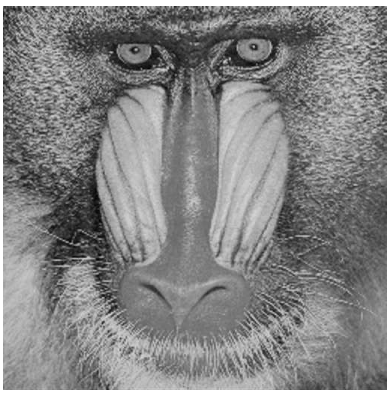

Figure 2.13: Original Mandril Image

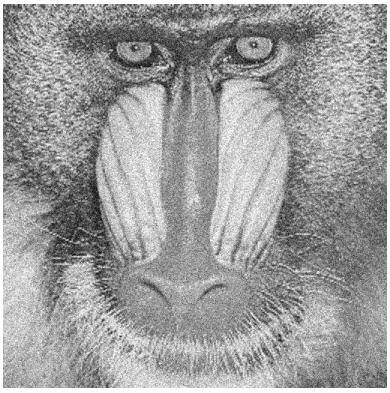

Figure 2.14: Snapshot of TV Flow at $t = 0$ with $h = 5E - 3$, PSNR=31.25

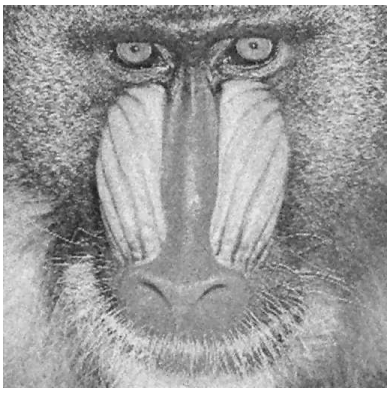

Figure 2.15: Snapshot of TV Flow at $t = 5E - 5$ with $h = 5E - 3$, PSNR=45.29

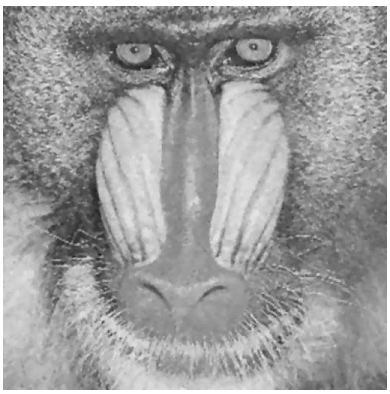

Figure 2.16: Snapshot of TV Flow at $t = 1E-4$ with $h = 5E-3$, PSNR=42.87

Figure 2.17: Snapshot of TV Flow at $t = 1.5E-4$ with $h = 5E-3$, PSNR=38.88

Figure 2.18: Snapshot of TV Flow at $t = 2E-4$ with $h = 5E-3$, PSNR=36.31

Chapter 3

Color Image Denoising

3.1 Introduction

As we described in Chapter 1, vector $\mathbf{I}(x) = (r(x), g(x), b(x))$ represents the intensity of the three primary colors. The chromaticity and brightness are produced from a color image by

$$\eta(x) := |\mathbf{I}(x)| \qquad \text{(brightness)}, \tag{3.1}$$

$$\mathbf{g} := \frac{\mathbf{I}(x)}{|\mathbf{I}(x)|} \qquad \text{(chromaticity)}, \tag{3.2}$$

where $|\mathbf{I}(x)|$ is the Euclidean norm of $\mathbf{I}(x)$. Therefore, the brightness $\eta(x)$ is the length of the RGB color vector and the chromaticity $\mathbf{g}$ denotes the normalized color component which must lie on the unit sphere $\mathbf{S}^2$ in $\mathbf{R}^3$ and the direction of this vector indicates the color. In this chapter, we use p-harmonic map to denoise the chromaticity of a given color image.

Let $\mathbf{u} : \Omega \subset \mathbf{R}^m \to \mathbf{S}^{n-1} \subset \mathbf{R}^n$ be a vector-valued function, where Ω is a bounded domain with smooth boundary $\partial\Omega$ and $\mathbf{S}^{n-1}$ denote the unit sphere in $\mathbf{R}^n$. We

consider the p-energy

$$E_p(\mathbf{u}) = \frac{1}{p}\int_\Omega |\nabla \mathbf{u}|^p \, dx, \qquad 1 \le p < \infty \tag{3.3}$$

for $\mathbf{u} \in C^1(\Omega, \mathbf{S}^{n-1})$. A map $\mathbf{u}$ is called a p-harmonic map if $\mathbf{u}$ is a minimizer of E_p. This is a constrained minimization problem with constraint $|\mathbf{u}| = 1$ a.e. in Ω.

The Euler-Lagrange equation of p-energy is (see Appendix A)

$$-\Delta_p \mathbf{u} = |\nabla \mathbf{u}|^p \mathbf{u}, \tag{3.4}$$

where

$$\Delta_p \mathbf{u} := \mathrm{div}(|\nabla \mathbf{u}|^{p-2} \nabla \mathbf{u}). \tag{3.5}$$

The operator Δ_p is often called the p-Laplacian [Che94, Mis01, Far02]. The equation (3.4) is a *singular elliptic* equation for $1 \le p < 2$, and a *degenerate elliptic* equation for $p > 2$. For $p = 2$, both degeneracy and singularity disappear.

We call a map $\mathbf{u} \in W^{1,p}(\Omega, \mathbf{S}^{n-1})$ a *weakly p-harmonic map* if $\mathbf{u}$ satisfies (3.4) in the sense of distribution, where $W^{1,p}(\Omega, \mathbf{S}^{n-1})$ denotes the Sobolev space

$$W^{1,p}(\Omega, \mathbf{S}^{n-1}) := \{\mathbf{u} \in W^{1,p}(\Omega, \mathbf{R}^n); \mathbf{u}(x) \in \mathbf{S}^{n-1} \text{ for a.e. } x \in \Omega\}.$$

Applying the gradient decent method, which is one of best-known methods for minimization problem, leads to considering the following gradient flow (or heat flow) for the p-energy functional E_p:

$$\mathbf{u}_t - \Delta_p \mathbf{u} = |\nabla \mathbf{u}|^p \mathbf{u} \qquad \text{in } \Omega_T := \Omega \times (0, T), \tag{3.6}$$

$$|\mathbf{u}| = 1 \qquad \text{in } \Omega_T, \tag{3.7}$$

complemented with some given boundary and initial conditions. It is easy to see that (3.6) is a *singular parabolic* equation for $1 \leq p < 2$ and a *degenerate parabolic* equation for $p > 2$. For $p = 2$, both degeneracy and singularity disappear.

The p-harmonic map and p-harmonic heat flow have been studied extensively in the past twenty years for $1 < p < \infty$. Chen [Che89] proved the existence of global weak solution for the harmonic flow in the case of the target manifolds are spheres using a penalization technique. Coron [Cor90] and *Hungerbühler* [Hun97] showed nonuniqueness of the p-harmonic flow. The p-harmonic map and p-harmonic flow appear in many scientific and engineering applications. For example, the harmonic map ($p = 2$) and its heat flow play a critical role in modeling liquid crystals and in micromagnetism. Image processing for denoising color images is another application of p-harmonic map and its heat flow for $1 \leq p < 2$. For instance, given the chromaticity $\mathbf{g}$ of a noisy color image, one method for recovering chromaticity $\mathbf{u}$ of color images using the p-harmonic map is defined as follows [Tan00, Ves02]:

$$\mathbf{u} = \underset{\mathbf{v} \in W_N^{1,p}(\Omega, \mathbf{S}^2)}{\operatorname{argmin}} J_{p,\lambda}(\mathbf{v}) \qquad \text{for } p \geq 1, \tag{3.8}$$

where

$$J_{p,\lambda}(\mathbf{v}) := E_p(\mathbf{v}) + \frac{\lambda}{2} \int_\Omega |\mathbf{v} - \mathbf{g}|^2 \, dx \qquad \text{for } \lambda > 0, \tag{3.9}$$

$$W_N^{1,p}(\Omega, \mathbf{S}^2) := \left\{ \mathbf{v} \in W^{1,p}(\Omega, \mathbf{S}^2); \frac{\partial \mathbf{v}(x)}{\partial \mathbf{n}} = 0 \text{ for a.e. } x \in \partial\Omega \right\}.$$

The most important and interesting cases are $1 \leq p < 2$ since the denoised images using these models are better at keeping geometric information such as edges and corners of the noisy color images. We call (3.8) the *p-harmonic model* for color image denoising, again, the parameter λ controls the trade-off between goodness of fit-to-fit-data and variability in $\mathbf{u}$.

3.2 The p-Harmonic Map Denosing Model

Again, motivated by the steepest descent method for solving (3.8), we consider the gradient flow (heat flow) for the energy functional $J_{p,\lambda}$ to find the solution for the p-harmonic model. The gradient flow for (3.9) is defined as [Bar]

$$\mathbf{u}_t - \Delta_p \mathbf{u} + \lambda(\mathbf{u} - \mathbf{g}) = \mu_{p,\lambda}\mathbf{u} \qquad \text{in } \Omega_T, \tag{3.10}$$

$$|\mathbf{u}| = 1 \qquad \text{in } \Omega_T, \tag{3.11}$$

$$\frac{\partial \mathbf{u}}{\partial \mathbf{n}} = 0 \qquad \text{on } \partial\Omega_T := \partial\Omega \times (0,T), \tag{3.12}$$

$$\mathbf{u} = \mathbf{u}_0 \qquad \text{on } \Omega \times \{t = 0\}, \tag{3.13}$$

where

$$\mu_{p,\lambda} := |\nabla \mathbf{u}|^p + \lambda(1 - \mathbf{u}\cdot\mathbf{g}).$$

There are two nonlinear terms in the p-harmonic flow equation, the first one is the p-Laplace term and the other one is the right hand side of (3.10) due to the nonconvex constraint $|\mathbf{u}| = 1$. To handle the degeneracy of the p-Laplace term, we approximate the p-energy $E_p(\mathbf{v})$ by the following regularized energy

$$\begin{aligned} E_p^\varepsilon(\mathbf{u}) &:= \frac{b_p(\varepsilon)}{2}\int_\Omega |\nabla \mathbf{v}|^2 \, dx + \frac{1}{p}\int_\Omega |\nabla \mathbf{v}|_\varepsilon^p \, dx \\ &= \int_\Omega \left\{ \frac{b_p(\varepsilon)}{2}|\nabla \mathbf{v}|^2 + \frac{1}{p}[\,|\nabla \mathbf{v}|^2 + a_p(\varepsilon)^2\,]^{\frac{p}{2}} \right\} dx, \end{aligned} \tag{3.14}$$

where $\varepsilon > 0$ and

$$a_p(\varepsilon) := \begin{cases} 0 & \text{if } 2 \le p < \infty, \\ \varepsilon & \text{if } 1 \le p < 2, \end{cases} \tag{3.15}$$

$$b_p(\varepsilon) := \varepsilon^\alpha \qquad \text{for } 1 \le p < \infty, \tag{3.16}$$

and some $\alpha > 0$ [Bar]. In the rest of this chapter, we use the shorthand notation

$$|\nabla \mathbf{v}|_\varepsilon := \sqrt{|\nabla \mathbf{v}|^2 + a_p(\varepsilon)^2}. \tag{3.17}$$

To handle the nonconvex constraint $|\mathbf{u}| = 1$ a.e., we approximate it by the well known Ginzburg-Landau penalization [Bet94], that is, instead of applying the exact constraint $|\mathbf{u}| = 1$ a.e., we enforce it approximately by adding a penalization term to the regularized p-energy E_p^ε, that is,

$$E_p^{\varepsilon,\delta}(\mathbf{v}) := E_p^\varepsilon(\mathbf{v}) + L^\delta(\mathbf{v}) \qquad \text{for } \varepsilon,\, \delta > 0, \tag{3.18}$$

where

$$L^\delta(\mathbf{v}) := \frac{1}{\delta}\int_\Omega F(\mathbf{v})dx, \qquad F(\mathbf{v}) := \frac{1}{4}(|\mathbf{v}|^2 - 1)^2 \qquad \forall\, \delta > 0,\, \mathbf{v} \in \mathbf{R}^n. \tag{3.19}$$

So the idea is, as ε gets smaller and smaller, the energy functional $E_p^{\varepsilon,\delta}$ becomes more and more favorable for maps $\mathbf{u}$ which take values close to the unit sphere $\mathbf{S}^{n-1}$ [Bar]. Therefore, the regularized model for the p-harmonic model (3.8) (with general m and n) is defined as

$$\mathbf{u} = \underset{\mathbf{v}\in W_N^{1,p}(\Omega,\mathbf{R}^n)}{\operatorname{argmin}} J_{p,\lambda}^{\varepsilon,\delta}(\mathbf{v}) \qquad \text{for } p \geq 1, \tag{3.20}$$

where

$$J_{p,\lambda}^{\varepsilon,\delta}(\mathbf{v}) := E_p^{\varepsilon,\delta}(\mathbf{v}) + \frac{\lambda}{2}\int_\Omega |\mathbf{v} - \mathbf{g}|^2\, dx. \tag{3.21}$$

The gradient flow for the regularized energy functional $J_{p,\lambda}^{\varepsilon,\delta}$ is given by

$$\mathbf{u}_t^{\varepsilon,\delta} - \Delta_p^{\varepsilon}\mathbf{u}^{\varepsilon,\delta} + \frac{1}{\delta}(|\mathbf{u}^{\varepsilon,\delta}|^2 - 1)\mathbf{u}^{\varepsilon,\delta} + \lambda(\mathbf{u}^{\varepsilon,\delta} - \mathbf{g}) = 0 \qquad \text{in } \Omega_T, \tag{3.22}$$

$$\frac{\partial \mathbf{u}^{\varepsilon,\delta}}{\partial \mathbf{n}} = 0 \qquad \text{on } \partial\Omega_T, \tag{3.23}$$

$$\mathbf{u}^{\varepsilon,\delta} = \mathbf{u}_0 \qquad \text{on } \Omega \times \{t = 0\}, \tag{3.24}$$

which is an approximation to the original flow (3.10)-(3.13). In the rest of this chapter, we define

$$\Delta_p^{\varepsilon}\mathbf{v} := b_p(\varepsilon)\Delta\mathbf{v} + \operatorname{div}(|\mathbf{v}|_{\varepsilon}^{p-2}\nabla\mathbf{v}) = \operatorname{div}\Big((b_p(\varepsilon) + [|\nabla\mathbf{v}|^2 + a_p^2(\varepsilon)]^{\frac{p-2}{2}})\nabla\mathbf{v}\Big). \tag{3.25}$$

The regularized flow (3.22)-(3.24) not only plays an important role for proving existence of weak solutions for the flow (3.10)-(3.13) but also provides a practical and convenient formulation for computing the solutions [Bar]. Barrett *et al.* [Bar] proved the well-posedness of (3.22)-(3.24), the energy law, a maximum principle, and some uniform (in ε and δ) a priori estimates. In addition, they proved the existence of global weak and classical solutions for the regularized flow (3.22)-(3.24), and the existence of global weak solutions for the flow (3.10)-(3.13) for $1 \le p < \infty$.

3.3 Finite Element Approximations for the p-Harmonic Map Heat Flow

In this section, we will discuss the finite element approximations for the p-harmonic heat flow. The convergence of the numerical solutions, as the spatial and temporal mesh sizes and the parameters ε and δ all tend to zero, of the gradient flow (3.10)-(3.13) will be summarized.

Remark 3.1. *We denote that* $\mathbf{u} = (u_1, u_2, u_3)$ *and* $\mathbf{g} = (g_1, g_2, g_3)$*. Each component of* $\mathbf{u}$ *and* $\mathbf{g}$ *corresponds to red, green and blue channel, respectively.*

Remark 3.2. *We will only construct fully discrete finite approximation schemes for* $m = 2$ *and* $n = 3$*, which is the case for image processing applications. However, our formulation and convergence analysis can be generalized to the case* $\Omega \subset \mathbf{R}^3$*, and* $n \geq 1$*.*

We will begin with a detailed derivation of the variational formulation, and then formulate the semi-discrete finite element approximation. At the end, we will introduce the fully discrete finite element discretization to compute the solutions of the p-harmonic flow (3.10)-(3.13) via (3.22)-(3.24).

Remark 3.3. *For notation brevity, we will consistently omit the indices* ε*,* δ *and* p *on* $\mathbf{u}$*.*

3.3.1 Variational Formulation

Let

$$\mathbf{V} = \Big\{ \mathbf{v} \in H^1(\Omega, \mathbf{R}^3); \frac{\partial \mathbf{v}}{\partial \mathbf{n}} = 0 \text{ on } \partial\Omega \Big\}.$$

To derive the variational formulation, first multiply (3.22) by a test function $\mathbf{v} \in \mathbf{V}$, then integrate over Ω we get

$$\begin{aligned} \int_\Omega \mathbf{u}_t \, \mathbf{v} - \int_\Omega \operatorname{div}\Big((b_p(\varepsilon) + |\nabla \mathbf{u}|_\varepsilon^{p-2}) \nabla \mathbf{u} \Big) \, \mathbf{v} + \frac{1}{\delta} \int_\Omega (|\mathbf{u}|^2 - 1) \mathbf{u} \, \mathbf{v} \\ + \lambda \int_\Omega (\mathbf{u} - \mathbf{g}) \, \mathbf{v} = 0. \end{aligned} \tag{3.26}$$

Note that we use (3.25) for the second term in (3.22). Applying Green's formula to the second term of (3.26), we get

$$\int_\Omega \mathbf{u}_t\,\mathbf{v} + \int_\Omega \mathcal{B}\cdot\nabla\mathbf{v} - \int_{\partial\Omega} \mathcal{B}n\cdot\mathbf{v} + \frac{1}{\delta}\int_\Omega (|\mathbf{u}|^2-1)\mathbf{u}\,\mathbf{v} + \lambda\int_\Omega (\mathbf{u}-\mathbf{g})\,\mathbf{v} = 0, \quad (3.27)$$

where

$$\mathcal{B} = [b_p(\varepsilon) + |\nabla\mathbf{u}|_\varepsilon^{p-2}]\nabla\mathbf{u}.$$

Since $\dfrac{\partial\mathbf{u}}{\partial\mathbf{n}} = 0$ on $\partial\Omega$, hence $\mathcal{B}n = 0$ on $\partial\Omega$, and (3.27) becomes

$$\int_\Omega \mathbf{u}_t\mathbf{v} + \int_\Omega \mathcal{B}\cdot\nabla\mathbf{v} + \frac{1}{\delta}\int_\Omega (|\mathbf{u}|^2-1)\mathbf{u}\,\mathbf{v} + \lambda\int_\Omega (\mathbf{u}-\mathbf{g})\,\mathbf{v} = 0. \quad (3.28)$$

Remark 3.4. *To avoid inconvenient subscripts,* $\dot{\mathbf{u}}$ *will be used to denote the time derivative* $\mathbf{u}_t$*.*

Our variational formulation to the p-harmonic flow (3.10)-(3.13) is defined as follows: Find $\mathbf{u}(\cdot,t) : [0,T] \to V$ such that $\mathbf{u} \in L^2((0,T);\,V)\cap H^1((0,T);\,L^2(\Omega))$ and

$$(\dot{\mathbf{u}},\mathbf{v}) + \mathbf{a}\,(\mathbf{u},\mathbf{v}) + \frac{1}{\delta}\,\mathbf{b}\,(\mathbf{u},\mathbf{v}) + \lambda(\mathbf{u}-\mathbf{g},\mathbf{v}) = 0 \qquad \forall\,\mathbf{v}\in\mathbf{V}, \quad (3.29)$$

$$(\mathbf{u}(\cdot,0),\mathbf{v}) = (\mathbf{u}_0(\cdot),\mathbf{v}) \qquad \forall\,\mathbf{v}\in\mathbf{V}, \quad (3.30)$$

where

$$\begin{aligned}
(\dot{\mathbf{u}},\mathbf{v}) &= \int_\Omega \frac{\partial\mathbf{u}}{\partial t}\,\mathbf{v},\\
\mathbf{a}\,(\mathbf{u},\mathbf{v}) &= \int_\Omega \mathcal{B}\cdot\nabla\mathbf{v},\\
\mathbf{b}\,(\mathbf{u},\mathbf{v}) &= \int_\Omega (|\mathbf{u}|^2-1)\mathbf{u}\,\mathbf{v},\\
(\mathbf{u}-\mathbf{g},\mathbf{v}) &= \int_\Omega (\mathbf{u}-\mathbf{g})\,\mathbf{v}.
\end{aligned}$$

The following existence theorem was proved in [Bar].

Theorem 3.1. *System (3.29)-(3.30) has a solution provided that* $|\mathbf{u}_0| \leq 1$ *and* $|\mathbf{g}| \leq 1$ *a.e. in* Ω. *Moreover, there exists a convergent subsequence of* $\{\mathbf{u}^{\varepsilon,\delta}\}$ *(still denoted by the same notation) whose limit (as* $\varepsilon, \delta \to 0$*)* $\mathbf{u}$ *is a global weak solution to (3.10)-(3.13).*

3.3.2 Semi-Discrete Finite Element Approximation

To define our finite element approximations for (3.29)-(3.30), let $\mathcal{T}_h = \{K_1, \ldots, K_{m_R}\}$ be a quasi-uniform triangulation of Ω of mesh size $h \in (0,1)$ and $\overline{\Omega} = \underset{K \in \mathcal{T}_h}{\cup} \overline{K}$. Since our triangulations are quasi-uniform, all elements K of $\mathcal{T}_h$ roughly have the same size. Our finite element space is defined as

$$\mathbf{V}_h := \{\mathbf{v} \in C^0(\overline{\Omega}, \mathbf{R}^3);\ \mathbf{v}_h|_K \in [P_1(K)]^3,\ \forall\, K \in \mathcal{T}_h\}.$$

Let $\mathcal{N}_h := \{p_i\}$, $(i = 1, \ldots, m_x)$ denote the set of all vertices of $\mathcal{T}_h$ and $\{\overrightarrow{\phi}_{j1}, \overrightarrow{\phi}_{j2}, \overrightarrow{\phi}_{j3}\} \in \mathbf{V}_h$, $(j = 1, \ldots, m_x)$ be a function corresponding to vertex p_i such that

$$\overrightarrow{\phi}_{j1} := \begin{pmatrix} \phi_j \\ 0 \\ 0 \end{pmatrix}, \quad \overrightarrow{\phi}_{j2} := \begin{pmatrix} 0 \\ \phi_j \\ 0 \end{pmatrix}, \quad \overrightarrow{\phi}_{j3} := \begin{pmatrix} 0 \\ 0 \\ \phi_j \end{pmatrix},$$

where

$$\phi_j(p_i) = \delta_{ij} \equiv \begin{cases} 1 & \text{if } i = j, \\ 0 & \text{if } i \neq j\ , \end{cases} \qquad i,\ j = 1, \ldots, m_x.$$

It can be shown that $\{\phi\}_{j=1,k=1}^{m_x,3}$ form a basis for $\mathbf{V}_h$, and

$$\mathbf{u}_h(\mathbf{x},t) = \sum_{i=1}^{m_x}\sum_{k=1}^{3} \xi_{ik}(t)\, \overrightarrow{\phi}_{ik}(\mathbf{x}) \qquad \forall\, \mathbf{x} \in \overline{\Omega}, \tag{3.31}$$

where $\xi_{ik}(t) = u_k^h(p_i,t)$. Then, our semi-discrete finite element method for (3.29)-(3.30) is defined as follows: Find $\mathbf{u}_h : [0,T] \to \mathbf{V}_h$ such that

$$(\dot{\mathbf{u}}_h, \mathbf{v}_h) + \mathbf{a}\,(\mathbf{u}_h, \mathbf{v}_h) + \frac{1}{\delta}\,\mathbf{b}\,(\mathbf{u}_h, \mathbf{v}_h) + \lambda(\mathbf{u}_h - \mathbf{g}, \mathbf{v}_h) = 0 \qquad \forall\, \mathbf{v}_h \in \mathbf{V}_h, \tag{3.32}$$

$$(\mathbf{u}_h(\cdot,0), \mathbf{v}_h) = (\mathbf{u}_0(\cdot), \mathbf{v}_h) \qquad \forall\, \mathbf{v}_h \in \mathbf{V}_h. \tag{3.33}$$

Substituting (3.31) and $\mathbf{v}_h = \overrightarrow{\phi}_{jk}$ into (3.32)-(3.33), then (3.32)-(3.33) becomes

$$\begin{aligned}
&\sum_{i=1}^{m_x}\sum_{k=1}^{3} \dot{\xi}_{ik}(t)(\overrightarrow{\phi}_{ik}(\mathbf{x}),\, \overrightarrow{\phi}_{jk}(\mathbf{x})) + \sum_{i=1}^{m_x}\sum_{k=1}^{3} \xi_{ik}(t)\hat{\mathbf{a}}(\overrightarrow{\phi}_{ik}(\mathbf{x}),\, \overrightarrow{\phi}_{jk}(\mathbf{x})) \\
&+ \frac{1}{\delta}\sum_{i=1}^{m_x}\sum_{k=1}^{3} \xi_{ik}(t)\,\hat{\mathbf{b}}\,(\overrightarrow{\phi_{ik}}(\mathbf{x}), \overrightarrow{\phi_{jk}}(\mathbf{x})) + \lambda \sum_{i=1}^{m_x}\sum_{k=1}^{3} \xi_{ik}(t)((\overrightarrow{\phi}_{ik}(\mathbf{x}) - \mathbf{g}),\, \overrightarrow{\phi}_{jk}(\mathbf{x})) = 0, \\
&j = 1, \ldots, m_x, \qquad t \in (0,T),
\end{aligned} \tag{3.34}$$

$$\sum_{i=1}^{m_x}\sum_{k=1}^{3} \xi_{ik}(0)(\overrightarrow{\phi}_{ik}(\mathbf{x}),\, \overrightarrow{\phi}_{jk}(\mathbf{x})) = (\mathbf{u}_0,\, \overrightarrow{\phi}_{jk}(\mathbf{x})), \qquad j = 1, \ldots, m_x. \tag{3.35}$$

Here,

$$\begin{aligned}
\hat{\mathbf{a}}(\overrightarrow{\phi}_{ik}(\mathbf{x}),\, \overrightarrow{\phi}_{jk}(\mathbf{x})) &= \int_\Omega \hat{\mathcal{B}} \cdot \nabla \overrightarrow{\phi}_{jk}(\mathbf{x}), \\
\hat{\mathcal{B}} &= [b_p(\varepsilon) + \sum_{i=1}^{m_x}\sum_{k=1}^{3} \xi_{ik}(t)\,|\nabla \overrightarrow{\phi}_{ik}(\mathbf{x})|_\varepsilon^{p-2}]\nabla \overrightarrow{\phi}_{ik}(\mathbf{x}), \\
\hat{\mathbf{b}}(\overrightarrow{\phi}_{ik}(\mathbf{x}),\, \overrightarrow{\phi}_{jk}(\mathbf{x})) &= \int_\Omega \Big(\Big| \sum_{i=1}^{m_x}\sum_{k=1}^{3} \xi_{ik}(t)\, \overrightarrow{\phi}_{ik}(\mathbf{x}) \Big|^2 - 1 \Big) \overrightarrow{\phi}_{ik}(\mathbf{x})\, \overrightarrow{\phi}_{jk}(\mathbf{x}).
\end{aligned}$$

(3.34)-(3.35) can be written in matrix form as

$$\mathbf{L}\,\dot{\xi}(t) + \Big\{\hat{\mathbf{A}} + \frac{1}{\delta}\,\hat{\mathbf{B}} + \lambda\,\mathbf{G}\Big\}\xi(t) = 0 \qquad \forall\, t \in (0,T), \tag{3.36}$$

$$\mathbf{L}\,\xi(0) = \chi, \tag{3.37}$$

where

$$\mathbf{L} = [\mathbf{L}_{\sigma\nu}], \qquad \mathbf{L}_{\sigma\nu} := (\overrightarrow{\phi}_{ik}, \overrightarrow{\phi}_{jk}), \tag{3.38}$$

$$\hat{\mathbf{A}} = [\hat{\mathbf{A}}_{\sigma\nu}(\xi(t))], \qquad \hat{\mathbf{A}}_{\sigma\nu}(\xi(t)) := \hat{\mathbf{a}}(\overrightarrow{\phi}_{ik}, \overrightarrow{\phi}_{jk}), \tag{3.39}$$

$$\hat{\mathbf{B}} = [\hat{\mathbf{B}}_{\sigma\nu}(\xi(t))], \qquad \hat{\mathbf{B}}_{\sigma\nu} := \hat{\mathbf{b}}(\overrightarrow{\phi}_{ik}, \overrightarrow{\phi}_{jk}), \tag{3.40}$$

$$\mathbf{G} = [\mathbf{G}_{\sigma\nu}], \qquad \mathbf{G}_{\sigma\nu} := (\overrightarrow{\phi}_{ik} - \mathbf{g}, \overrightarrow{\phi}_{jk}), \tag{3.41}$$

$$\chi = (\chi_1, \cdots, \chi_{3m_x})^T, \qquad \chi_\nu := (\mathbf{u}_0, \overrightarrow{\phi}_{jk}), \tag{3.42}$$

$$\sigma = (i-1)3 + k, \qquad i = 1, \cdots, m_x, \quad k = 1,2,3, \tag{3.43}$$

$$\nu = (j-1)3 + j, \qquad j = 1, \cdots, m_x, \quad l = 1,2,3, \tag{3.44}$$

and

$$\xi(t) = [\xi_{11}(t), \xi_{12}(t), \xi_{13}(t), \cdots, \xi_{(3m_x)1}(t), \xi_{(3m_x)2}(t), \xi_{(3m_x)3}(t)]^T. \tag{3.45}$$

(3.36)-(3.37) is a nonlinear ODE system in $\xi(t)$. In the next section, we will describe the time discretization of (3.32) and address convergence of our fully discrete finite element approximations.

3.3.3 Fully Discrete Finite Element Approximation

To formulate the fully discrete finite element approximations, we decompose the density function F, which is not a convex, into the difference of two convex functions W_+ and W_-, that is,

$$F(\mathbf{v}) = W_+(\mathbf{v}) - W_-(\mathbf{v}).$$

One such example is $W_+ = \dfrac{|\mathbf{v}|^4}{4}$ and $W_- = \dfrac{|\mathbf{v}|^2}{2} - \dfrac{1}{4}$. Obviously, this decomposition is not unique. It is easy to see that $(|\mathbf{u}|^2 - 1)\mathbf{u}$ in (3.26) is $\nabla F(\mathbf{u})$. Using $\nabla F(\mathbf{v}) = \nabla W_+(\mathbf{v}) - \nabla W_-(\mathbf{v})$, we can decompose $\mathbf{b}(\mathbf{u}_h, \mathbf{v}_h)$ in (3.32) into

$$\mathbf{b}(\mathbf{u}_h, \mathbf{v}_h) = \mathbf{b}_+(\mathbf{u}_h, \mathbf{v}_h) - \mathbf{b}_-(\mathbf{u}_h, \mathbf{v}_h),$$

where

$$\begin{aligned} \mathbf{b}_+(\mathbf{u}_h, \mathbf{v}_h) &:= (\nabla W_+(\mathbf{u}_h), \mathbf{v}_h), \\ \mathbf{b}_-(\mathbf{u}_h, \mathbf{v}_h) &:= (\nabla W_-(\mathbf{u}_h), \mathbf{v}_h). \end{aligned}$$

Let $J_\tau := \{t\}_{s=0}^{m_T}$ be a quasi-uniform partition of $[0, T]$ with mesh size $\tau := \dfrac{T}{m_T}$, and $\partial_t \mathbf{v}^k := \dfrac{\mathbf{v}^k - \mathbf{v}^{k-1}}{\tau}$. Then, our fully discrete finite element discretization for the initial boundary value problem (3.22)-(3.24) is defined as follows: Find $\mathbf{u}_h^k \in \mathbf{V}^h$ for $k = 1, \cdots, m_T$ such that

$$\begin{aligned} (\partial_t \mathbf{u}_h^k, \mathbf{v}_h) + \mathbf{a}(\mathbf{u}_h^k, \mathbf{v}_h) + \lambda(\mathbf{u}_h^k - \mathbf{g}, \mathbf{v}_h) \\ + \frac{1}{\delta}\, \mathbf{b}_+(\mathbf{u}_h^k, \nabla \mathbf{v}_h) = \frac{1}{\delta} \mathbf{b}_-(\mathbf{u}_h^{k-1}, \mathbf{v}_h) \forall\, \mathbf{v}_h \in \mathbf{V}_h, \end{aligned} \tag{3.46}$$

$$(\mathbf{u}_h^0(\cdot), \mathbf{v}_h) = (\mathbf{u}_0(\cdot), \mathbf{v}_h) \qquad \forall\, \mathbf{v}_h \in \mathbf{V}_h, \tag{3.47}$$

where

$$\begin{aligned}
(\partial_t \mathbf{u}_h^k, \mathbf{v}_h) &= \int_\Omega \partial_t \mathbf{u}_h^k \, \mathbf{v}_h, \\
\mathbf{a}(\mathbf{u}_h^k, \mathbf{v}_h) &= \int_\Omega \mathcal{B}_h^k \cdot \nabla \mathbf{v}_h, \\
\mathbf{b}_+(\mathbf{u}_h^k, \mathbf{v}_h) &= \int_\Omega \nabla W_+(\mathbf{u}_h^k)\, \mathbf{v}_h, \\
\mathbf{b}_-(\mathbf{u}_h^{k-1}, \mathbf{v}_h) &= \int_\Omega \nabla W_-(\mathbf{u}_h^{k-1})\, \mathbf{v}_h, \\
(\mathbf{u}_h^k - \mathbf{g}, \mathbf{v}_h) &= \int_\Omega (\mathbf{u}_h^k - \mathbf{g})\, \mathbf{v}_h.
\end{aligned}$$

Since equation (3.46) is a nonlinear equation in $\mathbf{u}_h^k$ for each k, the above numerical method is an implicit scheme. In matrix notation, (3.46) becomes

$$\Big\{\mathbf{L} + \tau\big(\hat{\mathbf{A}} + \frac{1}{\delta}\,\hat{\mathbf{B}}_+ + \lambda\,\mathbf{G}\big)\Big\}\xi^k = \big(\frac{\tau}{\delta}\,\hat{\mathbf{B}}_- + \mathbf{L}\big)\xi^{k-1}, \tag{3.48}$$

where ξ_{il}^k is an approximation to $\xi_{il}(t_k)$. For the fully discrete finite element solution $\mathbf{u}_h^k$, we define its linear interpolation in t as

$$\begin{aligned}
\mathbf{U}^{\varepsilon,\delta,h,\tau}(\cdot,t) :=& \frac{t - t_{k-1}}{\tau}\mathbf{u}_h^k(\cdot) + \frac{t_{k-1} - t}{\tau}\mathbf{u}_h^{k-1}(\cdot) \\
& \forall\, t \in [t_{k-1}, t_k], \quad 1 \le s \le m_T.
\end{aligned} \tag{3.49}$$

It is obvious that $\mathbf{U}^{\varepsilon,\delta,h,\tau}$ is continuous in both x and t. The following theorem [Bar] shows the convergence of the numerical solution to the weak solution of (3.22)-(3.24).

Theorem 3.2. *Let $\Omega \subset \mathbf{R}^m$ be a bounded domain with Lipschitz boundary. For $1 \le p < \infty$, suppose that $\mathbf{u}_0 \in L^\infty((0,T); W^{1,p*}(\Omega, \mathbf{R}^n))$, $p* := \max\{2, p\}$, $|\mathbf{u}_0| \le 1$, and $|\mathbf{g}| \le 1$ a.e. in Ω. For each pair of positive numbers (ε, δ), let $\mathbf{u}^{\varepsilon,\delta}$ denote the unique weak solution of (3.22)-(3.24) and $\mathbf{U}^{\varepsilon,\delta,h,\tau}$ be defined by (3.49). Then, there*

holds

$$\lim_{h,\tau\to 0} \|\mathbf{u}^{\varepsilon,\delta} - \mathbf{U}^{\varepsilon,\delta,h,\tau}\|_{L^q}(\Omega_T) = 0 \qquad \forall\, q \in [1,\infty). \tag{3.50}$$

The last theorem [Bar] verifies the convergence of the numerical solution to a weak solution $\mathbf{u}$ of (3.10)-(3.13).

Theorem 3.3. *, Let* $1 \le p < \infty$, $\mathbf{U}^{\varepsilon,\delta,h,\tau}$ *be defined by (3.49), and* $\mathbf{u}$ *be a weak solution of (3.10)-(3.13). Then, there exists a subsequence of* $\{\mathbf{U}^{\varepsilon,\delta,h,\tau}\}$ *(still denoted by the same notation) such that*

$$\lim_{\varepsilon,\delta\to 0}\lim_{h,\tau\to 0} \|\mathbf{u} - \mathbf{U}^{\varepsilon,\delta,h,\tau}\|_{L^q}(\Omega_T) = 0 \qquad \forall\, q \in [1,\infty). \tag{3.51}$$

3.4 Numerical Tests

In this section, we present some the numerical tests for the p-harmonic map heat flow model with $p = 1$. Similar to the procedure used in Section 2.4, in each test to be given below, we add a "salt & pepper" noise with noise density 0.02 to the original test image to produce a noisy image $\mathbf{g}$, we then use the p-harmonic map heat flow model to remove the noise and to get a denoised image $\mathbf{u}$. For numerical tests, we used $\lambda = 5$ and time step $k = 1E-5$. The same measurement PSNR is used to judge the quality of the denoised image. PSNR for color image can be calculated by

$$PSNR = 10\log_{10}\Big(\frac{MAX^2}{(MSE(R) + MSE(G) + MSE(B))/3}\Big),$$

Figure 3.1 is Lena image without noise. Figure 3.2 shows Lena image with "salt & pepper" noise with noise density 0.02. We used Figure 3.2 for the initial condition. Figure 3.3 is a snapshot at $t = 2E-4$, which still has noise. Snapshot in Figure 3.4

Figure 3.1: Original Lena Image

Figure 3.2: Snapshot of 1-harmonic Map Flow at $t = 0$ with $h = 7E-3$, PSNR=23.47

Figure 3.3: Snapshot of 1-harmonic Map Flow at $t = 2E - 4$ with $h = 7E - 3$, PSNR=15.82

Figure 3.4: Snapshot of 1-harmonic Map Flow at $t = 5E - 4$ with $h = 7E - 3$, PSNR=15.98

has noise but it is already a bit denoised. Most of noise is removed in Figure 3.5. We can notice that all the noise in Figure 3.6 is removed at $t = 1E - 3$.

Figure 3.5: Snapshot of 1-harmonic Map Flow at $t = 7E - 4$ with $h = 7E - 3$, PSNR=15.88

Figure 3.6: Snapshot of 1-harmonic Map Flow at $t = 1E - 3$ with $h = 7E - 3$, PSNR=15.85

Chapter 4

Generalized Model

In this Chapter, we first introduce a generalized model of the p-harmonic map model for color image denosing. We then present some numerical tests for the generalized model. Finally, we compare numerical tests from Section 3.4 with those obtained by channel-by-channel model.

4.1 Generalizations

For a given noisy chromaticity $\mathbf{g}$, our generalized model seeks

$$\mathbf{u} = \underset{\mathbf{v}\in W_N^{1,1}(\Omega,\mathbf{S}^{n-1})}{\operatorname{argmin}} \mathcal{J}_{\beta,\lambda}(\mathbf{v}), \tag{4.1}$$

where

$$\mathcal{J}_{\beta,\lambda}(\mathbf{v}) := \beta\,\mathcal{E}_{\varphi}(\mathbf{v}) + \frac{\lambda}{q}\int_{\Omega} |\mathbf{v}-\mathbf{g}|^q\,dx \qquad \text{for } \beta>0,\ \lambda\geq 0,\ 1\leq q<\infty, \tag{4.2}$$

$$\mathcal{E}_{\varphi}(\mathbf{v}) := \int_{\Omega} \varphi(|\nabla \mathbf{v}|)\,dx, \tag{4.3}$$

and the energy density function $\varphi : \mathbf{R}_+ \cup \{0\} \to \mathbf{R}_+$ is a real-valued, continuous, nondecreasing, convex, and linear growth function [Fen06]. Some examples of such density functions are

$$\varphi(s) = s \qquad \forall\, s \in \mathbf{R}_+ \cap \{0\}, \tag{4.4}$$

and

$$\varphi(s) = \sqrt{s^2 + 1} \qquad \forall\, s \in \mathbf{R}_+ \cap \{0\}, \tag{4.5}$$

which is known as minimal surface energy density. It is easy to verify that a solution of (4.1) with (4.4) and $q = 2$ is the 1-*harmonic map* model, which was discussed in Chapter 3. The Euler-Lagrange equation of (4.1) is given by [Fen06]

$$-\beta\, \mathrm{div}\mathcal{B} + \lambda|\mathbf{u} - \mathbf{g}|^{q-2}(\mathbf{u} - \mathbf{g}) = \mu_{\beta,\lambda}\mathbf{u} \qquad \text{in } \Omega, \tag{4.6}$$

$$|\mathbf{u}| = 1 \qquad \text{a.e. in } \Omega, \tag{4.7}$$

$$\mathcal{B}\mathbf{n} = 0 \qquad \text{on } \partial\Omega, \tag{4.8}$$

where

$$\mathcal{B} := \frac{\varphi'(|\nabla \mathbf{u}|)}{|\nabla \mathbf{u}|}, \qquad \mu_{\beta,\lambda} := \beta\varphi'(|\nabla \mathbf{u}|)|\nabla \mathbf{u}| + \lambda|\mathbf{u} - \mathbf{g}|^{q-2}(1 - \mathbf{u}\cdot\mathbf{g}).$$

Again, the gradient descent method motivates us to consider the following gradient flow for the energy functional $\mathcal{J}_{\beta,\lambda}$

$$\mathbf{u}_t - \beta\, \mathrm{div}\mathcal{B} + \lambda|\mathbf{u} - \mathbf{g}|^{q-2}(\mathbf{u} - \mathbf{g}) = \mu_{\beta,\lambda}\mathbf{u} \qquad \text{in } \Omega_T, \tag{4.9}$$

$$|\mathbf{u}| = 1 \qquad \text{a.e.in } \Omega_T, \tag{4.10}$$

$$\mathcal{B}\mathbf{n} = 0 \qquad \text{on } \partial\Omega_T := \partial\Omega \times (0, T), \tag{4.11}$$

$$\mathbf{u} = \mathbf{u}_0 \qquad \text{on } \Omega_0 = \Omega \times \{t = 0\}, \tag{4.12}$$

where $\mathbf{u}_0$ is some given initial map and $\varphi'(s)$ denotes the derivative of $\varphi(s)$.

We use the same techniques as those used in Chapter 3 to handle the degeneracy of the leading term in (4.9) and the nonconvex constraint $|\mathbf{u}| = 1$, we then introduce the following regularized variation problem as an approximation to (4.1)

$$\mathbf{u} = \operatorname*{argmin}_{\mathbf{v}\in W_N^{1,1}(\Omega,\mathbf{R}^n)} \mathcal{J}_{\beta,\lambda}^{\varepsilon,\delta}(\mathbf{v}) \qquad \text{for } \varepsilon,\ \delta > 0, \tag{4.13}$$

where

$$\mathcal{J}_{\beta,\lambda}^{\varepsilon,\delta}(\mathbf{v}) := \beta\mathcal{E}_{\varphi}^{\varepsilon,\delta}(\mathbf{v}) + \frac{\lambda}{q}\int_\Omega |\mathbf{v}-\mathbf{g}|^q\ dx, \tag{4.14}$$

$$\mathcal{E}_{\varphi}^{\varepsilon,\delta}(\mathbf{v}) := \frac{\varepsilon^2}{2}\int_\Omega |\nabla\mathbf{v}|^2\ dx + \int_\Omega \varphi(|\nabla\mathbf{v}|_\varepsilon)\ dx + \mathcal{L}^\delta(\mathbf{v}), \tag{4.15}$$

and $\mathcal{L}^\delta(\mathbf{v})$ is same as (3.19). Finally, the gradient flow for the regularized energy functional $\mathcal{J}_{\beta,\lambda}^{\varepsilon,\delta}$ is given by [Fen06]

$$\mathbf{u}_t^{\varepsilon,\delta} - \beta\varepsilon^\alpha\ \Delta\mathbf{u}^{\varepsilon,\delta} - \beta\,\mathrm{div}\Big(\frac{\varphi'(|\nabla\mathbf{u}^{\varepsilon,\delta}|_\varepsilon)}{|\nabla\mathbf{u}^{\varepsilon,\delta}|_\varepsilon}|\nabla\mathbf{u}|^{\varepsilon,\delta}\Big) \tag{4.16}$$

$$+\lambda|\mathbf{u}^{\varepsilon,\delta}-\mathbf{g}|^{q-2}(\mathbf{u}^{\varepsilon,\delta}-\mathbf{g}) + \frac{\beta}{\delta}(|\mathbf{u}^{\varepsilon,\delta}|^2-1)\mathbf{u}^{\varepsilon,\delta} = 0 \qquad \text{in } \Omega_T, \tag{4.17}$$

$$\mathcal{B}^{\varepsilon,\delta}\mathbf{n} = 0 \qquad \text{on } \partial\Omega_T, \tag{4.18}$$

$$\mathbf{u}^{\varepsilon,\delta} = \mathbf{u}_0 \qquad \text{on } \Omega_0. \tag{4.19}$$

Fully discrete finite element approximation schemes can be derived similarly as in Chapter 3. Here, we present numerical tests for the generalized model.

4.2 Numerical Tests

The following images are numerical tests for (4.17)-(4.19) and $q = 1$ and with (4.5) and $q = 1$,which are compared with the results obtained by the 1-*harmonic map* and by the channel-by-channel models. For the channel-by-channel model, we use the TV flow model to denoise each channel.

First four Figures 4.1, 4.2, 4.3, and 4.4 are snapshots of (4.17)-(4.19) with (4.4) and $q = 1$ at four different time steps. As t gets larger, noise is gradually removed. Figures 4.5, 4.6, 4.7, and 4.8 show snapshots of the flow with (4.5) and $q = 1$. Finally, numerical tests for the channel-by-channel model using the TV flow to denoise each channel are shown in Figure 4.9 to Figure 4.12. We observed that edges in the images are smeared when noise is totally removed.

Figure 4.1: Snapshot of (4.4) with $q = 1$ at $t = 2E - 4$, PSNR=15.87

Figure 4.2: Snapshot of (4.4) with $q = 1$ at $t = 5E - 4$ with $h = 7E - 3$, PSNR=15.95

Figure 4.3: Snapshot of (4.4) with $q = 1$ at $t = 7E - 4$ with $h = 7E - 3$, PSNR=15.98

Figure 4.4: Snapshot of (4.4) with $q = 1$ at $t = 1E-3$ with $h = 7E-3$, PSNR=15.81

Figure 4.5: Snapshot of (4.5) with $q = 1$ at $t = 2E-4$ with $h = 7E-3$, PSNR=15.81

Figure 4.6: Snapshot of (4.5) with $q = 1$ at $t = 5E-4$ with $h = 7E-3$, PSNR=15.83

Figure 4.7: Snapshot of (4.5) with $q = 1$ at $t = 7E-4$ with $h = 7E-3$, PSNR=15.82

Figure 4.8: Snapshot of (4.5) with $q = 1$ at $t = 1E-3$ with $h = 7E-3$, PSNR=15.60

Figure 4.9: Snapshot of Channel-by-Channel at $t = 1E-4$ with $h = 7E-3$, PSNR=25.58

Figure 4.10: Snapshot of Channel-by-Channel at $t = 3E - 4$ with $h = 7E - 3$, PSNR=25.18

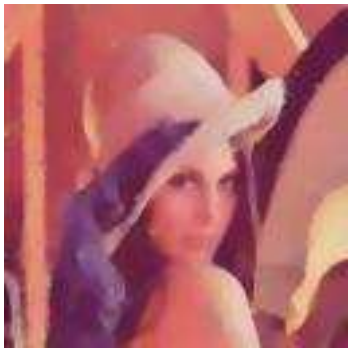

Figure 4.11: Snapshot of Channel-by-Channel at $t = 5E - 4$ with $h = 7E - 3$, PSNR=23.77

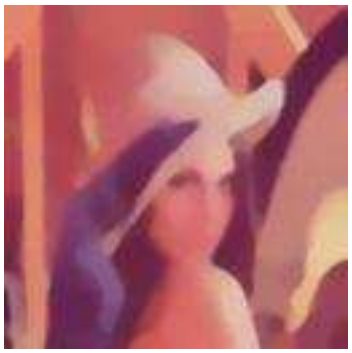

Figure 4.12: Snapshot of channel-by-channel at $t = 1E - 3$ with $h = 7E - 3$, PSNR=15.60

Bibliography

Bibliography

[Bar] J. W. Barrett, X. Feng, and A. Prohl, "p-harmonic map heat flow for $1 \leq p < \infty$ and their finite element approximations with applications to image processing", submitted .

[Bet94] F. Bethuel, H. Brezis, and F. Helein, *Ginzburg-Landau Vertices*, Birkhauser, New York, 1994.

[Blo98] P. V. Blomgren and T. F. Chan, "Color TV: Total variation methods for restoration of vector valued images", IEEE Trans. Image Processing **7**, 304 (1998).

[Bov05] A. Bovik, *Handbook of Image & Video Processing*, Elsevier, 2005.

[Cha97] A. Chambolle and P.-L. Lions, "Image recovery via total variation minimization and related problems", Numer. Math. **76**, 167 (1997).

[Cha01] T. F. Chan, S. H. Kang, and J. Shen, "Total variation denoising and enhancement of color images based on the CB and HSV color models", Journal of Visual Communucation and Image Representation **12**, 422 (2001).

[Cha02] T. Chan and J. Chen, "On the role of the BV image model in image restoration", Tech. Reprot, Department of Mathematics, UCLA **Cam 02-14**, 9 (2002).

[Che89] Y. Chen, "The weak solutions to the evolution problem of harmonic maps", Math. Z. **201**, 69 (1989).

[Che94] Y. Chen, M.-H. Hong, and N. Hungerbühler, "Heat flow of p-harmonic maps with values into spheres", Math. Z. **215**, 25 (1994).

[Cor90] J.-M. Coron, "Nonuniqueness for the heat flow of harmonic maps", Ann. Inst. H. Poincare **7**, 335 (1990).

[Eva02] L. C. Evans, *Partial Differential Equations*, AMS, 2002.

[Far02] A. Fardoun and R. Regbaoui, "Heat flow for p-harmonic maps between compact Riemannian mainfolds", Indiana Math. J. **40**, 1305 (2002).

[Fen06] X. Feng, "Divergence-L^q and divergence-measure tensor fields and gradient flow for linear growth functionals of maps into spheres", submitted .

[Fen03] X. Feng and A. Prohl, "Analysis of total variation flow and its finite element approximations", Math. Mod. Num. Analysis **37**, 533 (2003).

[Fen05] X. Feng, M. von Oehsen, and A. Prohl, "Rate of convergence of regularization procedures and finite element approximations for the total variation flow", Numer. Math. **100**, 441 (2005).

[Ger80] C. Gerhardt, "Evolutionary surfaces of prescribed mean curvature", J. Differential Equations **36**, 139 (1980).

[Giu84] E. Giusti, *Minimal Surfaces and Functions of Bounded Variation*, Birkhauser Verlag, Berlin, 1984.

[Gon04] R. C. Gonzalez, R. E. Woods, and S. L. Eddins, *Digital Image Processing using MATLAB®*, Prentice Hall, 2004.

[Hun97] N. Hungerbühler, "Nonuniqueness for the p-harmonic flow", Canad. Math. Bull **40**, 793 (1997).

[Lic78] A. Lichnewsky and R. Temam, "Pseudosolution of the time-dependent minimal surface problem", J. Differential Equations **30**, 340 (1978).

[Mis01] M. Misawa, "Approximathion of p-harmonic maps by penalized equation", Nonl. Analysis **47**, 1069 (2001).

[Rud92] L. Rudin, S. Osher, and E. Fatemi, "Nonlinear total variation based noise removal algorithms", Phys. D. **60**, 259 (1992).

[Sap96] G. Sapiro and D. Ringach, "Anisotropic diffusion of multivalued images with applications to color filtering", IEEE Trans. Image Processing **5**, 1582 (1996).

[Tan00] B. Tang, G. Sapiro, and V. Caselles, "Diffusion of general data on non-flat manifolds via harmonic maps theory: the direction diffusion case", Int. J. Comp. Vision **36**, 149 (2000).

[Ves02] L. Vese and S. Osher, "Numerical methods for p-harmonic flows and applications to image processing", SIAM J. Numer. Anal. **40**, 2085 (2002).

Appendix

Appendix A

We derive the Euler-Lagrange equation of the p-energy in the case of $p = 2$. Consider the problem of minimizing the energy

$$I[\mathbf{w}] = \frac{1}{2}\int_{\Omega} |\nabla \mathbf{w}|^2 \, dx \tag{A.1}$$

over all functions belonging to the admissible class

$$\mathcal{A} := \{\mathbf{w} \in H^1(\Omega;\, \mathbf{R}^n) |\ |\mathbf{w}| = 1 \ a.e.\} = H^1(\Omega;\, \mathbf{R}^n) \cap \mathbf{S}^{n-1}. \tag{A.2}$$

For any two same size matrices $A = [a_{ij}]$ and $B = [b_{ij}]$, we define $A : B = \sum_{i,j} a_{ij} b_{ij}$. The following theorem [Eva02] shows Euler-Lagrange equation of harmonic maps.

Theorem A.1. *Let* $\mathbf{u} \in \mathcal{A}$ *satisfy*

$$I[\mathbf{u}] = \min_{\mathbf{w} \in \mathcal{A}} I[\mathbf{w}].$$

Then

$$\int_{\Omega} \nabla \mathbf{u} : \nabla \mathbf{v} \, dx = \int_{\Omega} |\nabla \mathbf{u}|^2 \mathbf{u} \cdot \mathbf{v} \, dx$$

for any $\mathbf{v} \in H^1(\Omega; \mathbf{R}^n) \cap L^\infty(\Omega; \mathbf{R}^n)$. *Furthermore,* $\mathbf{u} = (u_1, \cdots, u_n)$ *is a weak solution of the boundary-value problem*

$$-\Delta \mathbf{u} = |\nabla \mathbf{u}|^2 \mathbf{u} \qquad \text{in } \Omega, \tag{A.3}$$

$$\frac{\partial \mathbf{u}}{\partial n} = 0 \qquad \text{on } \partial\Omega. \tag{A.4}$$

Proof. 1. Fix $\mathbf{v} \in H^1(\Omega; \mathbf{R}^n) \cap L^\infty(\Omega; \mathbf{R}^n)$. Then since $|\mathbf{u}| = 1$ a.e., we have $|\mathbf{u} + \tau\mathbf{v}| \neq 0$ a.e. for each sufficiently small τ. Consequently,

$$\mathbf{v}(\tau) := \frac{\mathbf{u} + \tau\mathbf{v}}{|\mathbf{u} + \tau\mathbf{v}|} \in \mathcal{A}. \tag{A.5}$$

Consider

$$i(\tau) := I[\mathbf{v}(\tau)].$$

Since $\mathbf{u}$ is a minimizer of $I[\cdot]$, we observe that $i(\cdot)$ has a minimum at $\tau = 0$. Therefore,

$$i'(0) = 0 \qquad \Big(\ ' = \frac{d}{d\tau} \Big). \tag{A.6}$$

2. Now

$$i'(0) = \int_\Omega \nabla \mathbf{u} : \nabla \mathbf{v}'(0)\, dx. \tag{A.7}$$

We compute directly from (A.5) that

$$\mathbf{v}'(\tau) = \frac{\mathbf{v}}{|\mathbf{u} + \tau\mathbf{v}|} - \frac{[(\mathbf{u} + \tau\mathbf{v}) \cdot \mathbf{v}](\mathbf{u} + \tau\mathbf{v})}{|\mathbf{u} + \tau\mathbf{v}|^3}. \tag{A.8}$$

Hence, $\mathbf{v}'(0) = \mathbf{v} - (\mathbf{u} \cdot \mathbf{v})\mathbf{u}$. Inserting this equality into (A.6), (A.7), we find

$$0 = \int_\Omega \{\nabla \mathbf{u} : \nabla \mathbf{v} - \nabla \mathbf{u} : \nabla((\mathbf{u} \cdot \mathbf{v})\mathbf{u})\}\, dx. \tag{A.9}$$

Since $|\mathbf{u}| \equiv 1$, we have

$$(\nabla \mathbf{u})^T \mathbf{u} = \mathbf{0}.$$

We then verify

$$\nabla \mathbf{u} : \nabla((\mathbf{u} \cdot \mathbf{v})\mathbf{u}) = |\nabla \mathbf{u}|^2 (\mathbf{u} \cdot \mathbf{v}) \qquad \text{a.e. in } \Omega.$$

Therefore,

$$\int_\Omega \nabla \mathbf{u} : \nabla \mathbf{v} \, dx = \int_\Omega |\nabla \mathbf{u}|^2 \mathbf{u} \cdot \mathbf{v} \, dx \qquad \forall \, \mathbf{v} \in H^1(\Omega; \mathbf{R}^n) \cap L^\infty(\Omega; \mathbf{R}^n). \tag{A.10}$$

3. Since

$$\begin{aligned} \int_\Omega \nabla \mathbf{u} : \nabla \mathbf{v} \, dx &= -\int_\Omega \Delta \mathbf{u} \cdot \mathbf{v} \, dx + \int_{\partial\Omega} \frac{\partial \mathbf{u}}{\partial n} \cdot \mathbf{v} \, ds \\ &= -\int_\Omega \Delta \mathbf{u} \cdot \mathbf{v} \, dx, \end{aligned} \tag{A.11}$$

(A.10) becomes

$$\int_\Omega (-\Delta \mathbf{u} - |\nabla \mathbf{u}|^2 \mathbf{u}) \cdot \mathbf{v} \, dx = 0 \qquad \forall \, \mathbf{v} \in H_0^1(\Omega; \mathbf{R}^n) \cap L^\infty(\Omega; \mathbf{R}^n).$$

Thus,

$$-\Delta \mathbf{u} = |\nabla \mathbf{u}|^2 \mathbf{u} \qquad \text{in } \Omega. \tag{A.12}$$

Finally, it follows from (A.10), (A.11), and (A.12) that

$$\int_{\partial\Omega} \frac{\partial \mathbf{u}}{\partial n} \cdot \mathbf{v} \, ds = 0 \qquad \forall \, \mathbf{v} \in H^1(\Omega; \mathbf{R}^n) \cap L^\infty(\Omega; \mathbf{R}^n).$$

Hence, $\frac{\partial \mathbf{u}}{\partial n} = 0$ a.e. on $\partial\Omega$. □

Remark A.1. *The function* $\lambda = |\nabla \mathbf{u}|^2$ *is the Lagrange multiplier corresponding to the pointwise constraint* $|\mathbf{u}| = 1$.

Appendix B

The following codes are written in Matlab®. To load an image in Matlab®, we use `I=imread('filename')`.

To add noise, we use `imnoise(I, 'noise type', mean of noise)`. All the functions for the numerical tests are listed below.

function name	description
`RGB`	Write each RGB channel of a color image as a gray image.
`CBC`	Combine RGB channel to generate a color image.
`NG`	Separate a color image into the brightness and the chromaticity components.
`DNI`	Combine RGB the brightness and the chromaticity components.
`cPSNR`	Compute PSNR for a color image.
`PSNR`	Compute PSNR for a gray image.

```
%%%%%%%%%%%%%%%%%%%%%%%%%%%%%%%%%%%%%%%%%%%%%%%%%%%%%%%%%%%%%%%%%%%%%%%%%%%%
function rgb=RGB(I)
% RGB separates RGB channel of color image and
% write each channel as a gray image.
%%%%%%%%%%%%%%%%%%%%%%%%%%%%%%%%%%%%%%%%%%%%%%%%%%%%%%%%%%%%%%%%%%%%%%%%%%%%
r=I(:,:,1); g=I(:,:,2); b=I(:,:,3);
imwrite(r,'rfilename.imagetype');
imwrite(g, 'gfilename.imagetype');
imwrite(b, 'bfilename.imagetype');
```

```
%%%%%%%%%%%%%%%%%%%%%%%%%%%%%%%%%%%%%%%%%%%%%%%%%%%%%%%%%%%%%%%%%%%%%%%%%%%%
function drgb=CBC(r,g,b)
% CBC combines RGB channels to generate a color image.
%%%%%%%%%%%%%%%%%%%%%%%%%%%%%%%%%%%%%%%%%%%%%%%%%%%%%%%%%%%%%%%%%%%%%%%%%%%%
[n,m]=size(r);
degb=zeros(n,m,3);
drgb(:,:,1)=r;
drgb(:,:,2)=g;
drgb(:,:,3)=b;
imwrite(drgb, 'filename.imagetype');
```

```
%%%%%%%%%%%%%%%%%%%%%%%%%%%%%%%%%%%%%%%%%%%%%%%%%%%%%%%%%%%%%%%%%%%%%%%%%%%%
function M=NG(I)
% NG breaks a color image into two parts which are the brightness
% and the chromaticity.
% Also, it saves results in certain format in order to import data to
% FEMLAB.
%%%%%%%%%%%%%%%%%%%%%%%%%%%%%%%%%%%%%%%%%%%%%%%%%%%%%%%%%%%%%%%%%%%%%%%%%%%%
cp=double(I);
g1=cp(:,:,1);
g2=cp(:,:,2);
g3=cp(:,:,3);
[n,m]=size(g1);
M=zeros(n,m);
for i=1:n
    for j=1:m
        if (g1(i,j)==0 & g2(i,j)==0 & g3(i,j)==0)
            M(i,j)=1;
        else
            M(i,j)=sqrt((g1(i,j))^2+(g2(i,j))^2+(g3(i,j))^2);
        end
    end
end
ng1=g1./M;
ng2=g2./M;
ng3=g3./M;
X=linspace(0,1.8,n);
```

```
Y=linspace(0,1.8,m);

nng1=[X;Y;ng1];

nng2=[X;Y;ng2];

nng3=[X;Y;ng3];

NM=[X;Y;M];

save Innr4.txt -ascii nng1

save Inng4.txt -ascii nng2

save Innb4.txt -ascii nng3

save Innm4.txt -ascii NM
```

```
%%%%%%%%%%%%%%%%%%%%%%%%%%%%%%%%%%%%%%%%%%%%%%%%%%%%%%%%%%%%%%%%%%%%%%%%%%%%
function DC=DNI(enr,eng,enb,enm)
% DNI combine the denoised brightness and chromaticity of image,
% then produces a color image.
%%%%%%%%%%%%%%%%%%%%%%%%%%%%%%%%%%%%%%%%%%%%%%%%%%%%%%%%%%%%%%%%%%%%%%%%%%%%
nm=double(enm);
nr=enr(3:end,:);
ng=eng(3:end,:);
nb=enb(3:end,:);
[n,m]=size(nr);
DC=zeros(n,m,3);
% scalar* vector
DR=nr.*nm;
DG=ng.*nm;
DB=nb.*nm;
% put RGB channel together
DC(:,:,1)=DR;
DC(:,:,2)=DG;
DC(:,:,3)=DB;
RI=uint8(DC);
imwrite(RI,'filename.imagetype');
```

```
%%%%%%%%%%%%%%%%%%%%%%%%%%%%%%%%%%%%%%%%%%%%%%%%%%%%%%%%%%%%%%%%%%%%%%%%%%%%
  function [cPSNR,mse]=cpsnr(X,Y)
% function [cPSNR,mse]=cpsnr(X,Y)
% cpsnr(X,Y) computes Peak signal to noise ratio of the
% difference between images and the
% mean square error of color image
% If the second input Y is missing then the PSNR and MSE of X itself
% becomes the output (as if Y=0).
%%%%%%%%%%%%%%%%%%%%%%%%%%%%%%%%%%%%%%%%%%%%%%%%%%%%%%%%%%%%%%%%%%%%%%%%%%%%
if nargin<2, D=X; else
   if any(size(X)~=size(Y)),
        error('The input size is not equal to each other!');
   end
   D=X-Y;
end D1=double(D); mse=sum(D1(:).*D1(:))/prod(size(X));
PSNR=10*log10(255^2/mse/3);
```

```
%%%%%%%%%%%%%%%%%%%%%%%%%%%%%%%%%%%%%%%%%%%%%%%%%%%%%%%%%%%%%%%%%%%%%%%
  function [PSNR,mse]=psnr(X,Y)
% function [PSNR,mse]=psnr(X,Y)
% psnr(X,Y) computes Peak signal to noise ratio of the difference
% between images and the mean square error of gray image.
% If the second input Y is missing then the PSNR and MSE of X itself
% becomes the output (as if Y=0).
%%%%%%%%%%%%%%%%%%%%%%%%%%%%%%%%%%%%%%%%%%%%%%%%%%%%%%%%%%%%%%%%%%%%%%%
if nargin<2, D=X; else
   if any(size(X)~=size(Y)),
        error('The input size is not equal to each other!');
   end
   D=X-Y;
end
D1=double(D);
mse=sum(D1(:).*D1(:))/prod(size(X));
PSNR=10*log10(255^2/mse)
```

Vita

Miun Yoon was born in Busan, Korea (Republic of) on February 6, 1980. After completing high school at Busan Jin girl's high school in 1998, she attended Dong-A University in Korea (March 1998 - February 2003), where she received her Bachelor of Science degree in Mathematics. During that period, she studied English in Canada for one year. She then entered the University of Tennessee at Knoxville in the fall of 2003. In December, 2006, she graduated from the University of Tennessee, Knoxville with a Master of Science degree in Mathematics. She is currently working towards her Ph.D. in Mathematics.